Thermo-Hydro-Mechanical Simulation of a TBM Tunnel in Clay Shale

Saeed Tourchi[1] and Arash Alimardani Lavasan*[1]

[1]Research Group Computational Soil Mechanics and Foundation Engineering (COMPSOIL), Department of Engineering, Faculty of Science, Technology and Medicine, University of Luxembourg, Luxembourg

Abstract

Tunnels in argillaceous weak rock formations such as Opalinus (OPA) shale, exhibit highly complex behavior due to coupled thermal, hydraulic, and mechanical (THM) processes. This study focuses on the New Belchen Tunnel (STB), excavated using a Tunnel Boring Machine (TBM) in faulted OPA shale. Previous field measurements and computational investigations demonstrated a strong relationship between temperature and radial pressure buildup around the tunnel. To address this, we numerically analysis the intermediate and long-term performance of the tunnel by modeling coupled interactions between temperature, pore pressure, and mechanical stress. A two-dimensional plane-strain coupled THM model is developed that captures stress and pore pressure profiles, considering tunnel excavation, stress redistribution, construction-induced heat release, and seasonal temperature fluctuations. The results highlight the importance of thermal expansion differences between the tunnel support and OPA shale, as well as temperature's critical influence on hydromechanical behavior, for accurate stress and deformation estimation over time. The model shows how exothermic reactions during concreting and seasonal temperature variations contribute to stress redistribution and pore pressure evolution in the soft rock mass. The coupled model effectively captures key THM interactions, illustrating how temperature-induced pore pressure reduces effective stress, potentially triggering fractures and swelling-driven deformation within the excavation-damaged zone (EDZ).

Keywords: Thermo-hydro-mechanical modeling; Deep tunnels; Opalinus clay shale; Ground-Tunnel interaction; Mechanized tunneling.

1 Introduction

The long-term performance and safety of underground structures in argillaceous formations, such as tunnels, geological repositories, and deep storage facilities, depend critically on under-

*Corresponding author: arash.lavasan@uni.lu

standing the coupled Thermo-Hydro-Mechanical (THM) behavior of the host geomaterial (Yu et al., 2010; Zhou et al., 2023; Mánica et al., 2022; Golchin et al., 2022; Bumbieler et al., 2021). Among the most studied formations in this regard is the Opalinus Clay (OPA), a Jurassic-aged claystone that has attracted extensive interest due to its low hydraulic conductivity, self-sealing capacity, and favorable geomechanical properties. These attributes have led to its selection as the reference host rock in Switzerland for deep geological disposal of high-level radioactive waste (Gens et al., 2007; Tsang et al., 2012), as well as its increasing relevance in tunnel infrastructure projects (Einstein and Bischoff, 1975; Madsen and Müller-Vonmoos, 1989; Einstein, 2000).

However, excavation in such materials, particularly by Tunnel Boring Machines (TBMs), disturbs the pre-existing stress equilibrium, initiating complex time-dependent processes in the surrounding rock mass. These include: (i) mechanical unloading and damage leading to stress redistribution; (ii) hydraulic gradients due to pore pressure changes and progressive resaturation; and (iii) thermal perturbations arising from construction processes, lining hydration, or environmental interaction. The resulting excavation damaged zone (EDZ) undergoes a gradual evolution influenced by the coupled interaction of these processes, often manifesting as delayed deformation, stress recovery, and volumetric changes including swelling (Bossart et al., 2017; Bossart, 2002; Gens, 2013). Historically, early analyses of tunnel stability emphasized mechanical and hydro-mechanical interactions (Einstein, 2000; Franzius and Pralle, 2011; Lavasan et al., 2018), under the assumption that thermal effects were negligible. Yet, as infrastructure is pushed deeper underground and as analogies from nuclear repository research are increasingly adopted in civil engineering, it is evident that thermal effects play a critical role in stress redistribution and material behavior (Gens, 2010; Tourchi et al., 2023; François et al., 2009).

In the case of Opalinus Clay, both laboratory and in-situ experimental programs, such as those at the Mont Terri Underground Rock Laboratory (Bossart and Thury, 2008; Bossart et al., 2017), have demonstrated that the material exhibits strong coupling between temperature, pore pressure, and mechanical behavior. Key features include: extremely low permeability, anisotropic stiffness and strength due to bedding orientation, time-dependent swelling, and thermally induced pore pressure changes under undrained conditions (Wild and Amann, 2018; Hueckel and Borsetto, 1990; Naumann et al., 2007; Favero et al., 2016; Monfared et al., 2014; Armand et al., 2004).These characteristics lead to behavior that cannot be accurately captured by simplified conventional models.

Despite this growing body of knowledge, real-world case studies combining long-term field monitoring with high-fidelity THM simulations remain rare, especially in TBM-excavated tunnels, where excavation is continuous and multi-physical interactions evolve simultaneously. A particularly relevant and well-documented case is the New Belchen Tunnel (STB) in the Swiss Jura Mountains (Grob, 1972; Amstad and Kovári, 2001). The STB tunnel intersects Opalinus Clay under overburdens up to 300 meters and was excavated using TBM technology alongside a comprehensive monitoring program (Ziegler et al., 2022, 2021). Radial pressures measured at the STB lining exhibited delayed increases post-excavation, suggestive of combined swelling and thermal effects. However, decoupling these effects to understand their individual contributions to stress evolution remains challenging. Understanding whether this pressure recovery is predominantly due to swelling (caused by resaturation) or to thermal expansion (resulting from

hydration heat or external thermal inputs) is essential for improving tunnel design, maintenance planning, and safety evaluations.

Field measurements revealed that the radial pressures acting on the tunnel support varied significantly (in a range of 0.5 to 1.5 MPa) and continued to increase over the four-year monitoring period (Ziegler et al., 2022). These pressures, considerably higher than those recorded in the old Belchen Tunnel, align with the laboratory-measured swelling potential of OPA shale and suggest a strong temperature effect induced by construction and annual air temperature cycles. For instance, the field measurements showed that during the setting process of gap grout and cast-in-place inner-lining, temperature fluctuations led to spikes in pressure. Additionally, a meaningful interrelation between monitored radial total pressures and seasonal air temperature during tunnel operation was observed.

As the intermediate material between the tunnel lining and host geological formation (i.e. OPA), the relatively soft bi-component grout utilized in this project was found to play a pivotal role in the thermal dynamics of the system (Ziegler and Loew, 2017, 2018). Although grout can retain heat, the temperature within the tunnel exhibits considerable variation contingent upon the season, typically being elevated in winter and reduced during summer. This seasonal fluctuation is significantly influenced by ventilation, which can introduce warm or cold air from the exterior into the tunnel cavity, resulting in temperature oscillations.

Furthermore, the heat generated from tunnel traffic adds complexity to the thermal environment, further complicating the thermal dynamics. These temperature variations can impact the structural integrity of the grout over time, especially if it becomes too soft or loses its mechanical properties due to prolonged exposure to high temperatures. The intangibility of the soft grout compared to stronger materials may lead to challenges in ensuring proper load transfer and stability, particularly in areas subjected to dynamic loads or temperature changes. Furthermore, temperature evolution in the vicinity of the tunnel not only impacts the mechanical behavior of the soft rock formation and lead to stress redistribution but also amplifies the thermal expansion mismatch between the concrete lining and the surrounding rock, generating additional stresses (Tourchi et al., 2023). Although this phenomenon has not been addressed in the literature, neglecting it in the design stage may threaten the structural integrity of the tunnel. Moreover, the temperatures variation in clay-rich shales with remarkably low permeability leads to evolution of pore pressure in the adjacent rock that affects the effective stress and correspondingly the shear strength of formation around the tunnel (Mohajerani et al., 2012; Monfared et al., 2011, 2014; Thoeny, 2014). This aspect can potentially induce fracture within the excavation damaged zone (EDZ). Over time, these stresses can result in cracking, debonding, and deformation of both the tunnel lining and the host rock.

Conventional numerical modeling tools, while capable of simulating mechanical deformation and pore pressure evolution, often neglect or oversimplify the thermal component. When thermal effects are included, they are typically represented as boundary conditions without fully accounting for their coupling to deformation and fluid transport. In contrast, fully coupled THM models, such as those implemented in the CODE_BRIGHT software (Olivella et al., 1996), offer a more rigorous approach for simulating the complex interactions that govern the behavior of claystone tunnel systems. However, such advanced models also require careful calibration,

robust numerical stability, and validation against field-scale data. Material properties of the OPA, such as thermal expansion coefficients, permeability anisotropy ratios, and constitutive model parameters for plastic flow, are highly variable and sensitive to both spatial location and stress path history (Armand et al., 2004; Bossart and Thury, 2011). Moreover, the evolution of the EDZ, which governs many of the boundary and transition zones in the model, is inherently nonlinear and poorly constrained. Thus, bridging the gap between theoretical modeling and practical application in the context of STB remains an open research question.

The primary objective of this study is to develop a comprehensive THM model of the New Belchen Tunnel, building on the foundational observational work from our previous study (Ziegler et al., 2022), which presented and discussed field data. While earlier efforts primarily focused on in-situ monitoring and initial observations, this research enhances the understanding of tunnel behavior through detailed numerical simulations, allowing for a deeper exploration of the coupled THM processes. This study simulates the long-term effects of temperature fluctuations, pore pressure evolution, and mechanical stress redistribution on tunnel lining behavior. By employing an advanced numerical framework, the research quantifies the influence of temperature during construction and operational phases on the structural integrity of the tunnel lining in faulted OPA shale. This approach provided new insights for improving tunnel design and maintenance strategies in similarly challenging geological environments. Furthermore, the insights developed herein are not limited to civil infrastructure. The approach and findings are directly applicable to deep radioactive waste geological disposal design, where similar processes of heat generation, clay swelling, and long-term stress redistribution dominate. Integrating thermally coupled simulations into design processes will be indispensable for robust prediction of system evolution over the operational and post-closure lifetimes.

2 Description of the new Belchen Tunnel

The New Belchen Tunnel (Sanierungstunnel Belchen, STB) is an advanced infrastructure project constructed to alleviate the recurring maintenance issues associated with the aging Belchen Tunnel tubes, originally excavated in the 1960s. Located in the Swiss Jura Mountains (Figure 1), the existing tunnels suffered significant damage due to the swelling behavior of the surrounding anhydrite-rich marls (Gipskeuper) and OPA shale, which caused severe deformation of the tunnel linings. The new tunnel, constructed between 2016 and 2017, was designed to address these challenges by implementing a modern tunneling method and advanced support structures.

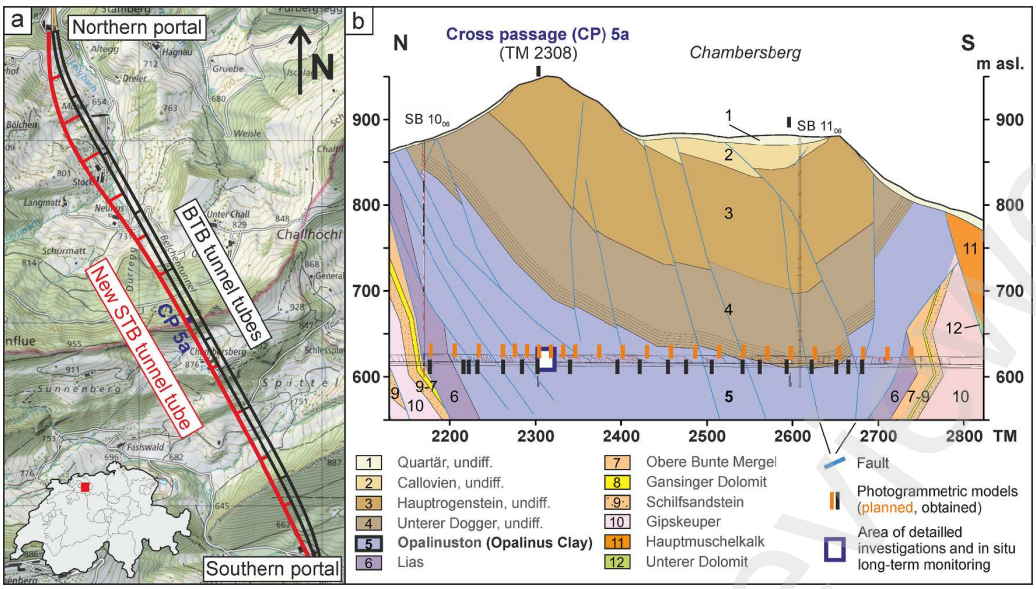

Figure 1: (a) Map view of the Belchen tunnel trajectories and location within Switzerland (b) Expected geological cross-section between TM 2130 and 2820 from North of the new Belchen Tunnel (Ziegler et al. 2022).

The STB is situated in a geologically complex area, traversing the folded and faulted formations of the Jura Mountain range, which includes Middle Triassic to Middle Jurassic sedimentary rocks. The geological conditions were well documented before construction, owing to the tunnel's proximity to the existing Belchen tunnel tubes (located 40–116 m laterally) and additional exploratory drillings conducted in 2006 and 2009. The tunnel route passes through the Upper Triassic Gipskeuper and the Aalenian to Toarcian OPA formations, both of which are known for their significant swelling potential.

The OPA shale, in particular, posed substantial challenges during tunnel construction. This formation, present in two distinct sections along the tunnel route, is part of the Chambersberg syncline. The shale's swelling behavior is exacerbated by its mineralogical composition, which includes a high proportion of sheet silicates, particularly illite/smectite interstratified clay minerals, known for their propensity to absorb water and expand. The geological complexity is further increased by the variable thickness of the OPA shale formation and the presence of steeply dipping faults and bedding planes, which caused frequent face instabilities during TBM excavation.

The STB has a total length of approximately 3.2 km and was excavated using a Tunnel Boring Machine (TBM), which provided a more controlled and continuous excavation process compared to the traditional drill-and-blast method used for the older tunnels. The TBM employed was a single-shield machine, about 75 m in length, with a shield length of 10 m. The choice of a TBM was strategic, as it allowed for minimal disturbance to the surrounding rock, reducing the extent of the excavation damage zone (EDZ) and thus limiting the ingress of water and the associated swelling risks. The tunnel's cross-section was designed with an excavated diameter of 13.97 m. The tunnel support system was carefully engineered to withstand the high swelling pressures expected from the surrounding rock formations. The primary support consists of a 35 cm-thick outer lining made of precast concrete segments arranged in rings with seven segments per ring. These segments are complemented by a drainage membrane and a 65

cm-thick inner cast-in-place concrete lining. The construction of the inner lining was staged to manage the stresses imposed on the structure: the invert (the bottom portion of the tunnel) was concreted approximately 375 m behind the TBM cutting face that corresponds to about 30 days after the excavation of section. In contrast, the sidewalls and crown support were completed around 1.15 km behind the cutting face that corresponds to about 140 days after cutting the face.

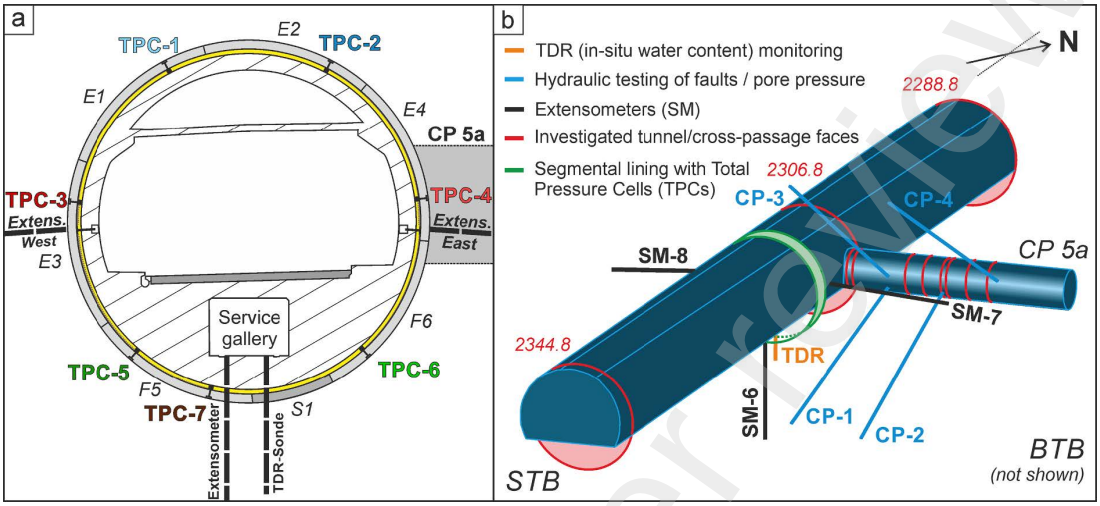

Figure 2: (a) Simplified 2D sketch of the monitoring section at TM 2317 with TPC-1–7, TDR borehole sonde in the tunnel invert, and three borehole extensometers. (b) 3D sketch of the monitoring section near the cross-passage (CP) 5a (Ziegler et al. 2022).

A crucial aspect of the tunnel's design was managing the annular gap between the excavated rock and the segmental lining. This gap was intentionally designed to be 22.5 cm wide and filled with a specially formulated two-component grout. The grout mixture, consisting of 90–95% cement-bentonite water, was injected immediately after the installation of the segments to provide both structural support and flexibility. This grout had a uniaxial compressive strength ranging from 1.7 to 3.2 MPa (Antonioli, 2018), and its mechanical properties were optimized to accommodate the deformation behavior of the swelling clay shale. The gap grout also played a crucial role in mitigating the risk of water-induced swelling by providing a barrier to groundwater movement. To reduce water pressure build-up on the tunnel lining and hinder drained formation waters to migrate along the tunnel into sections of swellable formations, drainage slots together with additional radial and longitudinal drainage membranes were installed at critical contacts of permeable and impermeable rock formations.

Extensive instrumentation was installed to monitor the tunnel's performance, particularly around tunnel meter (TM) 2317, where the overburden reached 325 m. This key monitoring section was equipped with instruments such as radial total pressure cells (TPC), borehole extensometers, and time-domain reflectometry (TDR) probes to measure mechanical pressure, radial deformations, and water content in the rock mass, respectively.

3 Characteristics of OPA shale

The OPA shale is a stiff, overconsolidated clay of the Lower Aalenian age, corresponding to the Middle Jurassic. It is found in the Jura Mountains of Northern Switzerland. Its mineralogy consists mainly of sheet silicates (illite, illitesmectite mixed layers, chlorites, kaolinites), framework silicates (albites, K-feldspar), carbonates (calcite, dolomite, ankerite, and siderite), and quartz (Bossart et al., 2002). There are three slightly different facies containing different mineral proportions: a shaly facies in the lower part of the deposit, a 15 m thick sandy-silty facies in the center, and a sandy facies interstratified with the shaly facies in the upper part. The content of clay minerals may range from 40% to 80%, depending on the facies. The clay was sedimented in marine conditions. Its pore water is highly mineralized, with total dissolved salts up to 20 g/l; this water contains a significant content of seawater millions of years old. The total thickness is about 160 m. As the OPA shale has been considered as the host rock for nuclear waste repository in the Switzerland, its behavior has been intensely studied through laboratory and in situ experimental programs originated from the Mont-Terrie Underground Rock Laboratory (URL). Table 1 presents the typical values for basic properties of OPA shale. The OPA shale consists of indurated clays of low porosity, low natural permeability, and higher strength.

Table 1: Some typical basic properties of OPA shale.

Property	**Value**
Dry density [g/cm^3]	2.22-2.33
Calcite content [%]	6-22
Porosity [%]	13.5-17.9
Water content [%]	4.2-8.0
Young's modulus [MPa]	4000-10000
Unconfined compression strength [MPa]	4-22
Hydraulic conductivity [m/s]	$1 - 5 \times 10^{-13}$

A synthesis of the main physical and geotechnical parameters obtained from various laboratory and in-situ measurements on OPA in Mont-Terrie URL is reported in Bossart and Thury (2011). Based on this information, the reference values of a series of parameters and their ranges have been listed in Table 2. Note that some of the parameters have different values depending on the orientation of the material, reflecting the anisotropy caused by the intense bedding of the clay. The quotation of a non-range refers to the scarcity of data for specific parameters.

Table 2: Reference parameters for OPA shale.

Properties	**Parameter**	**Orient.**	**Ref. value**	**Range**
Mineralogy	Clay content: %	-	62	44-80
	Carbonate content: %	-	14	6-22
	Quartz content: %	-	18	10-27
Petrophysical	Density, ρ: g/cm^3	-	2.45	$\pm$0.03
	Water content, w: %	-	6.1	$\pm$1.9
	Porosity, ϕ: %	-	15.7	$\pm$2.2
Mechanical	Uniaxial compression strength, R_c: MPa	$\parallel$	10	$\pm$6
		$\perp$	16	$\pm$6
	Tensile strength, R_t: MPa	$\parallel$	1	-
		$\perp$	0.5	-
	Elastic modulus, E: MPa	$\parallel$	10000	$\pm$3700
		$\perp$	4000	$\pm$1000
	Poisson's ratio, ν	$\parallel$	0.24	-
		$\perp$	0.33	-
	Shear strength parameters c': MPa	$\parallel$	5	$\pm$2
		$\perp$	2.2	$\pm$2
	Φ': degrees	$\parallel$	25	$\pm$3
		$\perp$	16.7	$\pm$3
Thermal/ thermo-mechanical	Thermal conductivity, λ: W/(mK)	$\parallel$	2.1	$\pm$10%
	Heat capacity of dry material at 20°C, E_s: J/(kg K)	$\perp$	0.995	$\pm$10%
	Coefficient of linear thermal expansion, α: K^{-1}	-	2.6×10^{-5}	-
Hydraulic/ hydro-mechanical	Water permeability of sound clay, m/s	-	10^{-13}	10^{-12} – 10^{-14}
	Biot's coefficient, b	-	0.6	0.42-0.78

At the STB location (Figure 2), the overburden is approximately 325m, and the closely spaced bedding dips at around 45°. In situ stress measurements have been carried out using borehole slotter, undercoring and hydraulic fracturing techniques, and have been supplemented by geological observations and the back-analysis of instrumented excavations; a comprehensive synthesis of these data is provided by Martin and Lanyon (2003). Among these methods, undercoring yields the most reliable estimates, as summarized in Table 3. These results indicate that the major principal stress is subvertical and closely corresponds to the overburden weight, the intermediate principal stress magnitude aligns well with hydraulic fracture test outcomes, and the relatively low minor principal stress concurs with the scarce occurrence of breakouts observed in vertical boreholes.

Table 3: Estimated in situ stress system (Gens et al., 2007).

Principal stress	Orientation	Azimuth: degrees	Dip: degrees	Value: MPa
Major, σ_1	Subvertical	N210	70	6.0-7.0
Intermediate, σ_2	Subhorizontal	N320	10	4.0-5.0
Minor, σ_3	Subhorizontal	N50	20	2.0-3.0

4 Theoretical formulation

4.1 THM formulation and balance equations

The theoretical THM formulation used for the simulation of STB is a particular case of the general formulation presented in Olivella et al. (1994) for saturated and unsaturated media. For space reasons, the formulation is only outlined in this section. Two phases are considered: solid (s) and liquid (l), corresponding to the two species of mineral and water (w). The solution of a coupled THM problem requires the simultaneous solution of the following balance equations:

Balance of solid:

$$\frac{\partial}{\partial t}[\rho_s(1-\phi)] + \nabla \cdot (j_s) = 0 \tag{1}$$

Balance of water mass:

$$\frac{\partial}{\partial t}(\rho_1 \phi) + \nabla \cdot (j_1) = f^w \tag{2}$$

Balance of internal energy:

$$\frac{\partial}{\partial t}[E_s \rho_s (1-\phi) + E_l \rho_1 S_1 \phi] + \nabla \cdot (i_c + j_E s + j_E l) = f^Q \tag{3}$$

Equilibrium:

$$\nabla \cdot \sigma + b = 0 \tag{4}$$

where ϕ is porosity; ρ is density; j is total mass flux; u is the solid displacement vector; σ is the stress tensor; b is the body forces vector; E is the specific internal energy; i_c is the conductive heat flux; and j_E is the energy flux due to mass motion.

Using the definition of the material derivative:

$$\frac{D_s(\cdot)}{Dt} = \frac{\partial(\cdot)}{\partial t} + \frac{du}{dt} \cdot \nabla(\cdot) \tag{5}$$

equation (1) becomes

$$\frac{D_s \phi}{Dt} = \frac{1}{\rho_s}\left[(1-\phi)\frac{D_s \rho_s}{Dt}\right] + (1-\phi)\nabla \cdot \frac{du}{dt} \tag{6}$$

Now, the solid mass balance can be eliminated by introducing it into the water mass balance relationship. Making use of the material derivative definition again, the following equation results:

$$\phi \frac{D_s \rho_w}{Dt} + \frac{\rho_w}{\rho_s}(1-\phi)\frac{D_s \rho_s}{Dt} + \rho_w \nabla \cdot \frac{du}{dt} + \nabla(\rho_w q_1) = 0 \tag{7}$$

The first two derivatives of this expression can be developed further, taking into account the dependences of the liquid and solid densities on temperature, solid pressure, and pore pressure, as follows:

$$\begin{cases} \rho_w = \rho_{w0} \exp\left[\beta_w (p_1 - p_{10}) + b_w T\right] \\ \rho_s = \rho_{s0} \exp\left[\beta_s (p_s - p_{s0}) + 3 b_s (T - T_{ref})\right] \end{cases} \tag{8}$$

where β_w and β_s are the water and solid compressibilities, respectively, and b_w and b_s are the volumetric and linear thermal expansion coefficients for water and the solid grain, respectively. Expanding the first two derivatives of equation (8) results in:

$$\left[\phi b_w + (1-\phi) 3 b_s\right] \frac{D_s T}{Dt} + \phi \beta_w \frac{D_s p_w}{Dt} + (1-\phi)\beta_s \frac{D_s p_s}{Dt} + \nabla \cdot \frac{du}{dt} + \frac{\nabla(\rho_w q_1)}{\rho_w} = 0 \tag{9}$$

Equation (9) contains the THM couplings that explain the variation of pore pressure when a temperature change is applied to the clay. The first term expresses the differential thermal expansion of the solid and liquid phases. The second and third terms represent the volume changes of the water and solid phases associated with a pore pressure change. The fourth term indicates the volume change of the material skeleton (including contributions from stresses, pore pressures, and temperature), and the fifth term is the volume change associated with the flow of water in or out of the element considered. The pore pressure generated will be the result of the interplay of all these terms in each particular case.

The formulation was completed with various constitutive laws that describe the phenomena under consideration. They have been presented and discussed elsewhere (e.g., Gens et al. (2017)). The main ones correspond to the flow of heat by conduction, the advective flow of water, and the mechanical constitutive law for mechanical behavior.

Heat conduction is governed by Fourier's law:

$$i_c = -\lambda \nabla T \tag{10}$$

where λ is the coefficient of thermal conductivity. Water flow is controlled by Darcy's law:

$$q_1 = -K_1(\nabla p_1 - \rho_w g) = -\frac{k}{\mu_l}(\nabla p_1 - \rho_w g) \tag{11}$$

where K_1 is the liquid permeability and k is the intrinsic permeability. Liquid permeability depends on temperature through the variation of water viscosity, and intrinsic permeability depends on porosity. In non-isothermal problems, it is more convenient to characterize the hydraulic conductivity of a material using the concept of intrinsic permeability.

4.2 Thermomechanical model for argillaceous hard soils–weak rocks

This section describes a constitutive model aimed at reproducing the main features of the THM behavior of the OPA shale. In particular, it incorporates non-isothermal anisotropy of strength and stiffness, nonlinear isotropic thermal hardening to compensate for plastic deformation before peak strength, thermal softening behavior after the peak, a non-associated flow rule, time-dependent deformation, and permeability dependency on plastic strains and temperature. The employed constitutive model for simulations was developed and implemented in CB by the first author in Tourchi et al. (2023). The model is implemented in terms of effective stresses, adopting the following generalized expression accounting for the effects of potential desaturation:

$$\sigma' = \sigma + S_e s B I \tag{12}$$

where σ' is the total stress tensor, S_e is the effective degree of saturation, s is the suction, B is Biot's coefficient, and I is the identity tensor.

4.2.1 Thermoelastic Components

The relationship between the elastic modulus (E) and temperature has been characterized by the following logarithmic function:

$$E(T) = E(T_0)\left[1 - \gamma \ln\left(\frac{T}{T_0}\right)\right] \tag{13}$$

where γ controls the rate of reduction of Young's modulus with temperature.

Assuming that the coefficient of thermal expansion is independent of stresses, the hypoelastic strain increment is defined as the sum of the thermal and mechanical components:

$$d\epsilon^e = d\epsilon^{(e,\sigma)} + \frac{1}{3} d\epsilon_v^{(e,T)} I \tag{14}$$

where $d\epsilon^{(e,\sigma)}$ is the increment of elastic strains caused by changes in effective stresses and $d\epsilon_v^{(e,T)}$ is the elastic volumetric strain increment caused by changes in temperature T. The latter can be defined as:

$$d\epsilon_v^{(e,T)} = 3\alpha_s dT \tag{15}$$

where α_s is the linear thermal expansion coefficient of the medium, which depends on the material mineralogy, temperature, and pressure changes, although it can be assumed constant for practical purposes.

4.2.2 Thermoplastic components

The total plastic strain increment in the thermoplastic constitutive model is formulated as the sum of instantaneous plastic deformations and time-dependent viscoplastic deformations, capturing both immediate and progressive responses of the OPA shale under thermal and mechanical loading

$$\mathrm{d}\varepsilon = \mathrm{d}\varepsilon^{\mathrm{ep}} + \mathrm{d}\varepsilon^{\mathrm{vp}} = \mathrm{d}\varepsilon^{\mathrm{ep}} + \mathrm{d}\dot{\boldsymbol{\varepsilon}}^{\mathrm{vp}} \tag{16}$$

where $d\epsilon_v^{(p,T)}$ is the total plastic strain increment that consists of the plastic strain increment $d\varepsilon^p$ and the viscoplastic strain rate tensor $\dot{\varepsilon}^{vp}$ in a time increment of dt. The strain rate viscoplastic tensor is computed as:

$$\dot{\varepsilon}^{\mathrm{vp}} = \frac{2}{3}\frac{\dot{\varepsilon}^{\mathrm{vp}}}{q}\mathbf{s} \tag{17}$$

$$q = \left(\frac{3}{2}\mathbf{s} : \mathbf{s}\right)^{1/2} \tag{18}$$

$$\varepsilon^{\mathrm{vp}} = \gamma \left\langle q - \sigma_{\mathrm{s}} \right\rangle^{n} \left(1 - \varepsilon_{\mathrm{eq}}^{\mathrm{vp}}\right)^{m} \tag{19}$$

where γ is a viscosity parameter, σ_s is a threshold from which viscoplastic strains are activated, $\langle\cdot\rangle$ are the Macaulay brackets, n and m are material constants, and ϵ_{eq}^{vp} is the state variable of the time-dependent mechanism, given by:

$$\varepsilon_{\mathrm{eq}}^{\mathrm{vp}} = \int_0^t \left(\frac{2}{3}\dot{\varepsilon}^{\mathrm{vp}} : \dot{\varepsilon}^{\mathrm{vp}}\right)^{1/2} \mathrm{d}t \tag{20}$$

4.2.3 Yield surface

Under low deviatoric stresses, the response is linearly elastic and characterized by a transversely isotropic form of Hooke's law. For higher deviatoric stress, plastic deformations develop on reaching the yield surface, characterized by generalized non-isothermal Mohr-Coulomb criterion:

$$f^T = \left(\cos\theta + \frac{1}{\sqrt{3}}\sin\theta\sin\varphi_{\mathrm{mob}}^T\right) J - \sin\varphi_{\mathrm{mob}}^T \left(c_{\mathrm{peak}}^{T_0}\ \cot\varphi_{\mathrm{mob}^T}\tan\varphi_{\mathrm{mob}^T}\cot\varphi_{\mathrm{mob}}^T + p\right) \tag{21}$$

where ϕ_{mob} is the mobilized friction angle, c_{mob} is the mobilized cohesion, and the remaining variables are stress invariants with their usual definitions. The friction angle varies in a piecewise manner as follows:

$$\phi_{mob}^{T} = \begin{cases} \phi_{\text{ini}} + \dfrac{\epsilon_{eq}^{p}}{a_{\text{hard}} - \dfrac{\epsilon_{eq}^{p}(a_{\text{hard}}-\xi_1)}{\xi_1}} & \text{if } \epsilon_{eq}^{p} \leq \xi_1 \\ \phi_{\text{peak}} & \text{if } \xi_1 < \epsilon_{eq}^{p} \leq \xi_2 \\ \phi_{\text{peak}} - \dfrac{\epsilon_{eq}^{p}-\xi_2}{a_{\text{soft}} - \dfrac{(a_{\text{soft}}-(\xi_3-\xi_2))}{(\phi_{\text{peak}}-\phi_{\text{res}})}\dfrac{(\epsilon_{eq}^{p}-\xi_2)}{(\xi_3-\xi_2)}} & \text{if } \xi_2 < \epsilon_{eq}^{p} \leq \xi_3 \\ \phi_{\text{res}} & \text{if } \epsilon_{eq}^{p} > \xi_3 \end{cases} \tag{22}$$

where ϕ_{ini} is the initial friction angle, ϕ_{peak} is the peak friction angle, ϕ_{res} is the residual friction angle, ϵ_{eq}^{p} is the state variable controlling hardening/softening, ξ_1 is the value of ϵ_{eq}^{p} at peak strength, ξ_2 is the value of ϵ_{eq}^{p} at which softening begins, ξ_3 is the value of ϵ_{eq}^{p} at which the residual strength is reached, a_{hard} is a parameter controlling the curvature of the function in the hardening branch, and a_{soft} is a parameter controlling the curvature of the function in the softening branch. The strength dependence on temperature is incorporated through parameters ϕ and c. In the case of the friction angle, the following equations are adopted to define ϕ_{ini}, ϕ_{peak}, ϕ_{res} as a function of temperature:

$$\phi_{\text{ini}}(T) = \phi_{\text{ini}}^{(T_0)} \left[1 - \mu_\phi \ln\left(\frac{T}{T_0}\right)\right] \tag{23}$$

$$\phi_{\text{peak}}(T) = \phi_{\text{peak}}^{(T_0)} \left[1 - \mu_\phi \ln\left(\frac{T}{T_0}\right)\right] \tag{24}$$

$$\phi_{\text{res}}(T) = \phi_{\text{res}}^{(T_0)} \left[1 - \mu_\phi \ln\left(\frac{T}{T_0}\right)\right] \tag{25}$$

where $\phi_{\text{ini}}^{(T_0)}$, $\phi_{\text{peak}}^{(T_0)}$, and $\phi_{\text{res}}^{(T_0)}$ are the initial, peak, and residual friction angles, respectively, at the reference temperature T_0, and μ_ϕ is a parameter controlling the rate of change of the friction angle with temperature. As in the case of mechanical loading, it is assumed that the Mohr-Coulomb envelope rotates around a fixed point, and therefore, we can define the temperature-dependent mobilized cohesion as:

$$c_{\text{mob}}(T) = c_{\text{peak}}^{(T_0)} \cot(\phi_{\text{peak}}^{(T_0)}) \tan(\phi_{\text{mob}}^{(T)}) \tag{26}$$

where $c_{\text{peak}}^{(T_0)}$ is the peak cohesion at the reference temperature T_0.

Figure 3 presents the mobilized friction angle as a function of temperature (T) and equivalent plastic strain (ϵ_{eq}^{p}). This 3D representation shows how the friction angles ϕ_{ini}, ϕ_{peak}, and ϕ_{res} vary with these parameters. At the initial temperature (T_0), the friction angle starts at ϕ_{ini}. As temperature and plastic strain increase, the friction angle evolves, reaching ϕ_{peak} and then ϕ_{res} before finally approaching the mobilized friction angle ϕ_{mob}.

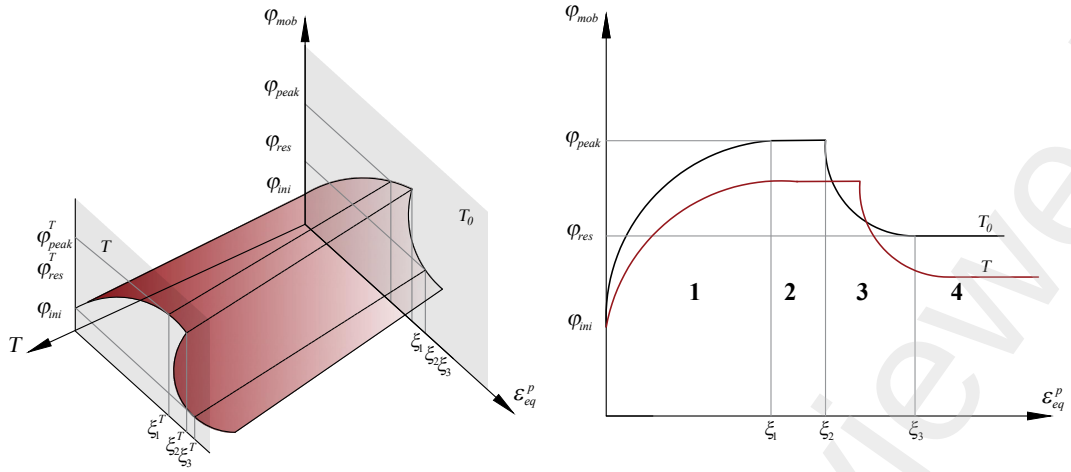

(a) **(b)**

Figure 3: (a) Evolution of the yield envelope; (b) Mobilised friction angle as a function of temperature and ϵ^p_{eq}.

4.2.4 Flow rule

Regarding the direction of plastic flow, a non-associated flow rule is adopted. Rather than deriving a specific function for the plastic potential, the flow rule is directly obtained from the yield criterion in the following way:

$$\frac{\partial g}{\partial \sigma} = \omega \left(\frac{\partial f}{\partial p}\frac{\partial p}{\partial \sigma} + \frac{\partial f}{\partial J}\frac{\partial J}{\partial \sigma} + \frac{\partial f}{\partial \theta}\frac{\partial \theta}{\partial \sigma} \right) \tag{27}$$

where g is the plastic potential function and ω is constant, controlling the volumetric component of plastic deformations. The increment of plastic deformations $d\epsilon^p$ is defined as:

$$d\epsilon^p = d\lambda \frac{\partial g}{\partial \sigma} \tag{28}$$

where λ is the plastic multiplier and is defined as:

$$d\lambda = \frac{1}{H}\left(\frac{\partial f}{\partial \sigma} d\sigma + \frac{\partial f}{\partial \phi_{\text{mob}}} \frac{\partial \phi_{\text{mob}}}{\partial T} dT \right) \tag{29}$$

$$H = -\frac{\partial f}{\partial \phi_{\text{mob}}} \frac{\partial \phi_{\text{mob}}}{\partial \epsilon^p_{eq}} \frac{\partial \epsilon^p_{eq}}{\partial \epsilon^p} \frac{\partial g}{\partial \sigma} \tag{30}$$

Therefore, plastic deformations are also affected by the thermal variation of the strength parameters. The model also accounts for cross-anisotropy (or transverse isotropy) through a non-uniform scaling of the stress tensor (Mánica et al., 2016):

$$\sigma^{ani} = \begin{bmatrix} \frac{\sigma^r_{11}}{c_N} & c_S\sigma^r_{12} & \sigma^r_{13} \\ c_S\sigma^r_{12} & c_N\sigma^r_{22} & c_S\sigma^r_{23} \\ \sigma^r_{13} & c_S\sigma^r_{23} & \frac{\sigma^r_{33}}{c_N} \end{bmatrix} \tag{31}$$

where c_N and c_S are respectively the normal and shear scaling factors in order to represent the anisotropy of the material, and σ^r_{ii} are the components of σ^r.

4.2.5 Hydro-mechanical components

The equivalent degree of saturation is given by the following form of the van Genuchten (1980) expression:

$$S_e = \frac{S_1 - S_{r1}}{S_{ls} - S_{r1}} = \left[1 + \left(\frac{p_g - p_1}{P}\right)^{\frac{1}{1-\lambda_t}}\right]^{\lambda_s} \tag{32}$$

where S_1 is the degree of saturation; S_{r1} is the residual degree of saturation; S_{ls} is the degree of saturation in saturated conditions (normally 1); p_g and p_1 are the gas and liquid pressures, respectively; λ_r is a shape function coefficient; and P can be interpreted as the air-entry pressure value. The model assumes that the intrinsic permeability evolves with plastic deformations to account for the observed permeability increase with damage in the OPA shale. The plastic multiplier λ is used to characterize the magnitude of the accumulated plastic deformations, and the intrinsic permeability tensor is defined by the following expression:

$$k = \begin{cases} k_0 e^{\eta(\lambda - \lambda_{\text{thr}})} & \text{if } \lambda > \lambda_{\text{thr}} \\ k_0 & \text{if } \lambda \leq \lambda_{thr} \end{cases} \tag{33}$$

where k_0 is the intrinsic permeability tensor of the intact rock, η is a constant that controls the rate of change, and λ_{thr} is a threshold value of λ from which permeability increases.

5 Numerical simulation

5.1 Simulation of the mechanical behavior of OPA shale

The constitutive model above has been applied to reproducing triaxial and creep tests performed on OPA shale samples. Parameters derived from this exercise are later applied to the analysis of a tunnel excavation. Temperature influence on the strength of the OPA shale was investigated in triaxial compression tests at elevated temperatures between 20°C and 115°C under undrained conditions. The samples were first isotropically loaded to about 3 MPa and then heated at a rate of 2 or 5°C/H to a desired level while the thermal expansion was measured. At constant lateral stress and temperature, the samples were axially loaded inclined to the bedding plane with angles of 30° to 40° by a strain rate of $1 \times 10^{-7}\,\text{s}^{-1}$.

Figure 4 shows the stress-strain curves obtained from the simulated triaxial and laboratory test results. Figure 5 shows the results in terms of volumetric strains. From both figures, a satisfactory agreement between the simulation results and the laboratory data can be noted. Table 4 summarizes the parameters of the mechanical and hydraulic constitutive model employed.

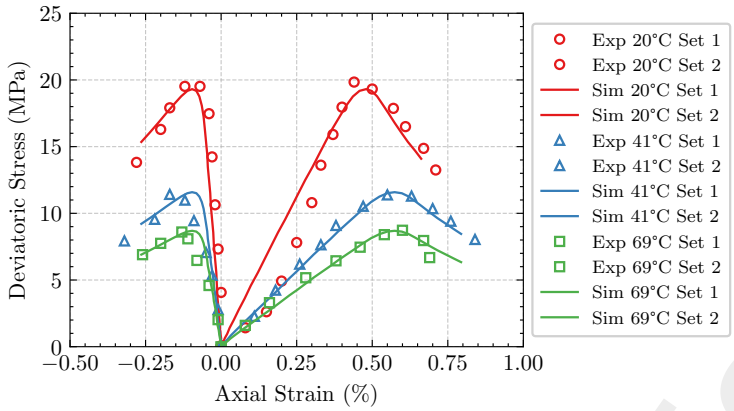

Figure 4: Stress-strain curves in triaxial tests on OPA shale. Observations (Zhang et al., 2007) and constitutive model results.

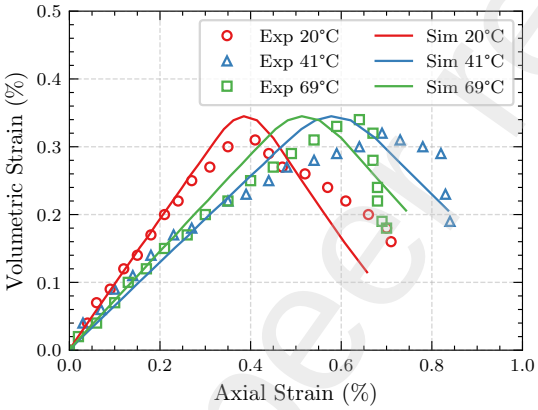

Figure 5: Volume change in triaxial tests on OPA shale. Observations (Zhang et al., 2007) and constitutive model results.

Table 4: Model parameters adopted for the simulation of the triaxial and creep tests.

Parameter	Units	Input value	Parameter	Units	Input value
Instantaneous mechanism			**Time-dependent mechanism**		
E_1, E_2	(MPa)	7200, 2800	σ_s	(MPa)	4.79
v_1, v_2	(–)	0.2	γ	(day^{-1})	9.69×10^{-6}
φ_{peak}	(°)	22	n	(–)	4.98
φ_{ini}	(°)	9.35	m	(–)	20
φ_{res}	(°)	14.74	**Hydraulic**		
c_{peak}	(MPa)	3.5	k_1, k_2	(m^2)	$1 \times 10^{-20}, 2 \times 10^{-20}$
a_{hard}	(–)	0.001	A	(–)	1
a_{soft}	(–)	0.05	Λ	(–)	3
ω	(–)	0.6	P	(MPa)	14.3
ξ_1	(–)	1×10^{-5}	λ	(–)	0.33
ξ_2	(–)	2×10^{-5}	**Thermal**		
ξ_3	(–)	9×10^{-3}	μ_ϕ	(–)	0.17
			μ_E	(–)	0.34

374 To investigate the significant rate-dependent behavior of OPA shale, creep tests have been

conducted under triaxial loading conditions in the literature (e.g. Naumann et al. 2007). In this case, controlled displacements were halted once the desired deviatoric stress was achieved, and from then on, the stress state was maintained constant for a specified duration. The experiments were performed at a constant confining pressure of 12 MPa, with triaxial loads increasing incrementally in stages. Each stage lasted up to 200 days, during which the differential stress was raised by increments of 2 MPa, starting from an initial value of 13 MPa. The tests aimed to observe the differences in creep behavior based on the orientation of the bedding planes in relation to the principal stress direction. Samples loaded parallel to the bedding planes (P-samples) demonstrated significantly different transient creep strains compared to those loaded normal to the bedding planes (S-samples). Figure 6 illustrates the results obtained in terms of time-dependent deformation. The parameters related to the time-dependent response are also provided in Table 4.

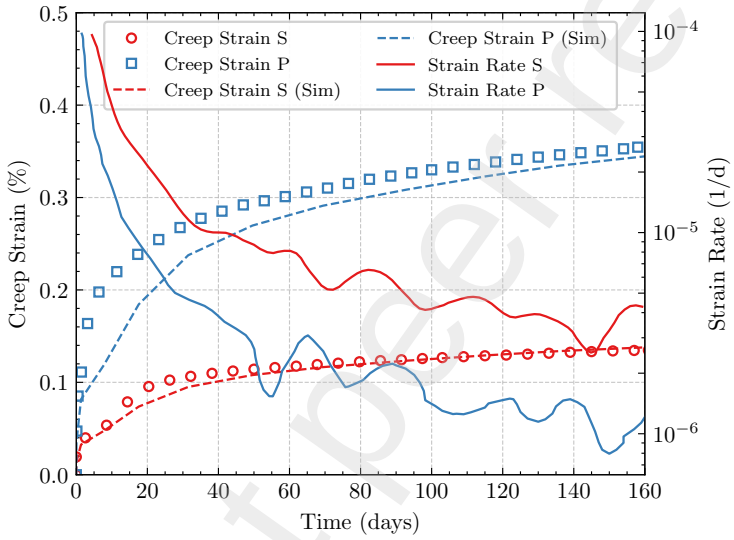

Figure 6: Creep tests on OPA shale. Test results (Naumann et al. 2007) and constitutive model results.

5.2 Aspect of analysis and material characteristics

In order to interpret the observed THM behavior of the STB, numerical simulations have been performed using finite element CODE–BRIGHT (Olivella et al., 1996). The model domain and the finite element mesh used are depicted in Figure 7, where the quasi-isotropic initial stress state can be noted. The initial vertical and horizontal principal stresses have been assumed to be 7 MPa and 5 MPa at the tunnel level, respectively (see Table 3). A hydrostatic distribution of water pressure was initially defined, with a value equal to the field value (1.35 MPa) at the test level. The dimensions of the model are 130 m × 130 m. The distance from the tunnel wall to the boundary is 58 m. Naturally, the model also incorporates the geometry of the liner and the gap grout between the liner and the OPA shale (Fig. Figure 7). The mesh contains 8745 quadrilateral elements and 8899 nodes; it has been refined near the gallery and the tunnel in order to effectively deal with the higher temperature and pore pressure gradients in this zone. An initial constant temperature of 13°C has been assumed throughout the geometry. The measured temperature variations were applied as a thermal boundary condition at the different measurement points on the liner.

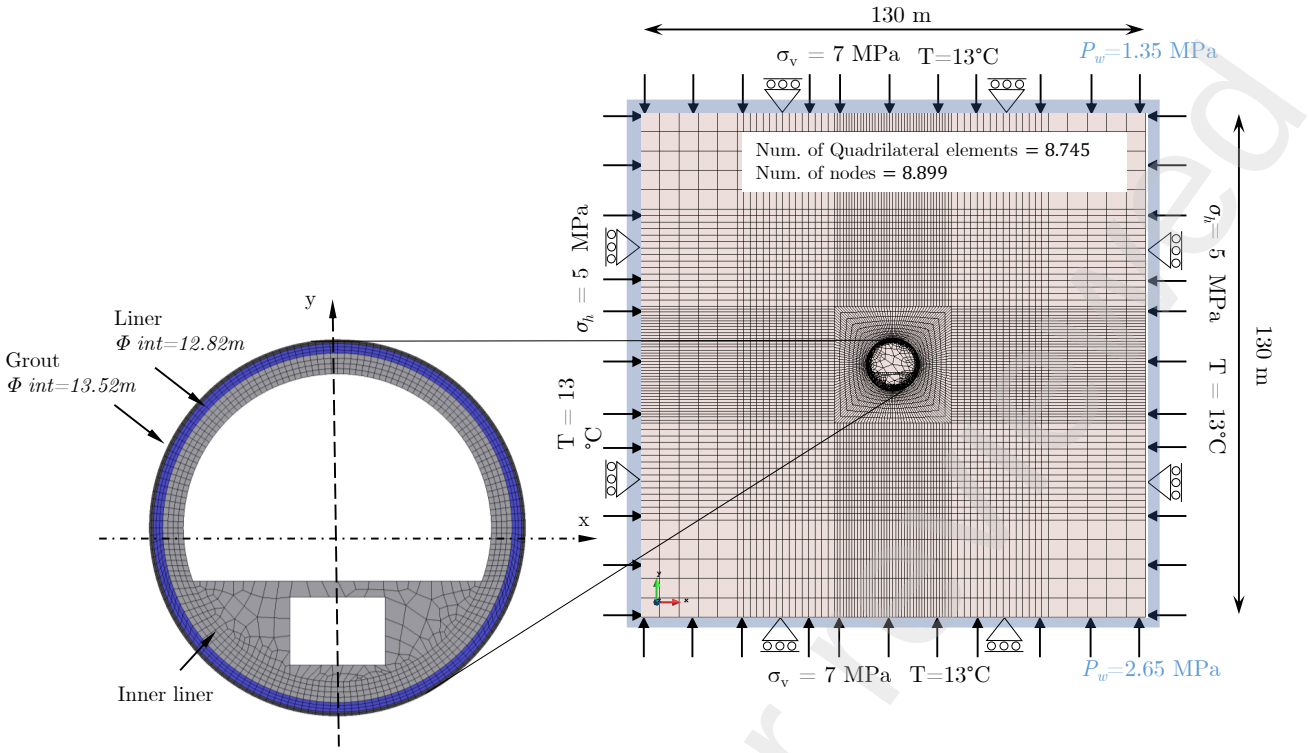

Figure 7: Geometry, Meshing and Initial and boundary conditions

The various stages of tunnel excavation were mimicked by the different phases of the numerical analysis as shown in the Table 5.

Table 5: Construction sequence of the New Belchen Tunnel at the monitoring section

Phase	**Start Date**	**End Date**	**Duration**
TBM excavation & precast lining	09 Feb 2016	21 Jun 2017	16 months
Annular-gap grouting (behind TBM shield)	Feb 2016	Jun 2017	16 months
Invert & service-tunnel segment concreting	01 Nov 2016	≈ 22 Nov 2016	∼3 weeks
Sidewalls & crown concreting	08 Apr 2017	08 Apr 2017	1 day
Cross-passage 5a excavation	mid-Jan 2017	mid-Jan 2017	∼1 week

Excavation was implemented by sequentially deactivating elements in a staged manner, corresponding to the progressive removal of material over discrete time intervals. This was achieved using the excavation/construction feature of CODE–BRIGHT, which allows the definition of material states via a control parameter. The construction stage activates the material gradually by linearly increasing its gravity during the assigned interval. To simulate excavation with stress relief in a numerically stable manner, the *smooth excavation mode* was employed. In this approach, elements transition from solid to inactive with a gradual reduction in stress, governed by a smooth stress relaxation law. The stress σ^t at time t during the excavation interval is computed as

$$\sigma^t = \sigma^{t_\mathrm{i}} \left(A - B \left[\frac{t - t_\mathrm{i}}{t_\mathrm{f} - t_\mathrm{i}} \right]^n \right), \tag{34}$$

where σ^{t_i} is the stress at the beginning of the interval, t_i and t_f are the initial and final times of the excavation interval, respectively, and A, B, and n are user-defined parameters. The parameter A (default value 1) controls the initial magnitude of stress relaxation. If $A < 1$, the relaxation starts from a reduced stress level. The parameter B (default value 1) determines the amplitude of stress decay, with lower values enabling partial relaxation. The exponent n (default value 1) controls the shape of the relaxation curve: $n > 1$ corresponds to accelerated decay, while $n < 1$ results in a decelerated stress release. Upon completion of the excavation interval, the affected elements automatically become inactive and are excluded from the subsequent calculations. This implementation enabled a stable and realistic simulation of excavation-induced stress redistribution and deformation, while maintaining fidelity to the coupled THM processes occurring in the surrounding geological medium.

The STB tunnel was excavated from south to north, with orientations suggesting a near east–west strike. The tunnel axis is approximately perpendicular to the bedding strike and intersects the southward-dipping layers at a steep angle (Figure 8). Consequently, the tunnel advances across anisotropic geological features, which significantly influence the stress redistribution and deformation behavior during and after excavation. The Opalinus Clay exhibits transversely isotropic behavior, with pronounced differences in stiffness along and across the bedding planes. Regarding the elastic stiffness anisotropy, a ratio between the horizontal and vertical Young's modulus of 2.57 was employed, consistent with the values reported in Bossart and Thury (2011). To estimate the effective elastic response along the tunnel's principal axes, the directional Young's modulus $E(\theta)$ was computed using the relation:

$$\frac{1}{E(\theta)} = \frac{\cos^2\theta}{E_\perp} + \frac{\sin^2\theta}{E_\parallel} \tag{35}$$

where θ is the angle between the axis of interest and the bedding normal. Assuming a bedding dip of 45° towards the south and a tunnel advancing from south to north, the effective Young's modulus was calculated for the longitudinal, vertical, and horizontal transverse directions (Table 6).

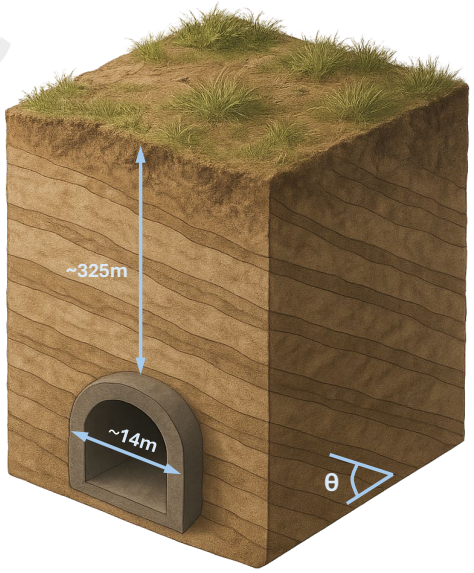

Figure 8: Schematic illustration of STB at the cross section near the cross-passage (CP) 5a.

Rock strength anisotropy was defined by adopting scaling factors $c_N = 1.33$ and $c_S = 1.0$, selected to obtain a reasonable configuration of the damaged zone. The variation of shear strength parameters with direction was approximated using a trigonometric interpolation approach. For a given angle θ measured from the bedding normal, the effective cohesion and friction angle were calculated using the following expressions:

$$c_{\text{eff}}(\theta) = c_{\perp} \cos^2 \theta + c_{\parallel} \sin^2 \theta \tag{36}$$

$$\phi_{\text{eff}}(\theta) = \phi_{\perp} \cos^2 \theta + \phi_{\parallel} \sin^2 \theta \tag{37}$$

where $c_{\perp}$ and $\phi_{\perp}$ represent the cohesion and friction angle perpendicular to bedding, and $c_{\parallel}$ and $\phi_{\parallel}$ are the corresponding values parallel to bedding. The angle θ is specific to the orientation of the tunnel axis relative to the bedding normal. The interpolated results for the tunnel's longitudinal, vertical, and horizontal directions are presented in Table 6.

Table 6: Directional mechanical parameters of OPA shale along tunnel axes

Tunnel Axis	**Young's Modulus**	**Cohesion**	**Friction Angle**
Longitudinal	4032	4.25	20.8°
Vertical	4032	4.25	20.8°
Horizontal	7200	4.90	24.9°

The constitutive model parameters used in the simulation are basically those obtained from the calibration of the constitutive model listed in Table 4. Moreover, Table 4 presents the intrinsic permeability of the intact rock, k_0, together with the parameter η, which quantitatively governs the nonlinear evolution of permeability as a function of the plastic multiplier.

5.3 Results of the analysis

The results from the numerical simulations are compared with field observations in this section. Figure 2 shows the location of the measurement points for the total radial pressure (TPC) and the temperature in a tunnel section. Seven radial total pressure cells (TPC-1 to TPC-7) were installed in specially designed steel-reinforced concrete lining segments, with the sensors placed at various positions around the tunnel circumference.

5.3.1 Temperatures and Total pressures

The combined analysis of temperature measurements and total pressure evolution from November 1, 2016, to November 1, 2017, highlights significant interactions and dependencies between thermal conditions and mechanical responses within the tunnel lining. Figure 9a presents both temperature measurements and total pressure data for TPC-1 and TPC-2. Initially, a sharp increase in both temperature and total pressure is observed, corresponding to early-stage construction activities such as lining installation and concrete curing. Notably, around day 150,

both temperature and total pressure exhibit pronounced peaks due to inverted concreting and service tunnel segment placement. The simultaneous rise in temperature (up to approximately 20°C above ambient) directly correlates with notable increases in total pressures, TPC-1 reaching about 1.5 MPa and TPC-2 approximately 0.9 MPa. This synchronous response underscores the strong thermal influence on mechanical stress variations, highlighting thermally induced expansion as a primary mechanism driving these pressures.

In the case of TPC-3 and TPC-4, shown in Figure 9b, temperature and total pressure variations further confirm this interaction. Both points initially experience rapid increases in temperature, coinciding with sharp rises in total pressure, particularly pronounced at TPC-4 around day 75 due to the excavation of cross-passage 5a. Subsequently, around day 150, another clear thermal peak (approximately 35°C) occurs, simultaneously triggering a total pressure peak at TPC-3 of about 1.2 MPa. This thermomechanical interplay illustrates how temperature changes induced by construction activities, particularly concrete curing and segmental lining placements, directly affect mechanical stress states within the tunnel lining. Measurements from TPC-5, TPC-6, and TPC-7 further illustrate the complexity of these interactions (Figure 9c). Initially, these points experience significant temperature spikes (up to 35°C) associated with early concrete curing reactions, leading to immediate increases in total pressure. Following this, both temperature and total pressures gradually decrease, stabilizing at lower levels as thermal conditions normalize. Notably, TPC-7 displays a different long-term trend, with a continuing rise in total pressure despite decreasing temperature, indicating other contributing factors such as rock swelling and additional mechanical influences.

This integrated temperature-pressure analysis emphasizes that construction-induced thermal processes substantially impact total pressure variations within tunnel linings. The numerical model predictions, while capturing general trends effectively, tend to underestimate the pressures at certain points, primarily due to simplified modeling assumptions and the exclusion of certain site-specific construction activities (e.g., cross-passage excavations). Despite these limitations, the clear correlation between measured temperatures and observed total pressures strongly supports the need to consider coupled thermal-mechanical interactions comprehensively during construction-phase modeling and analysis.

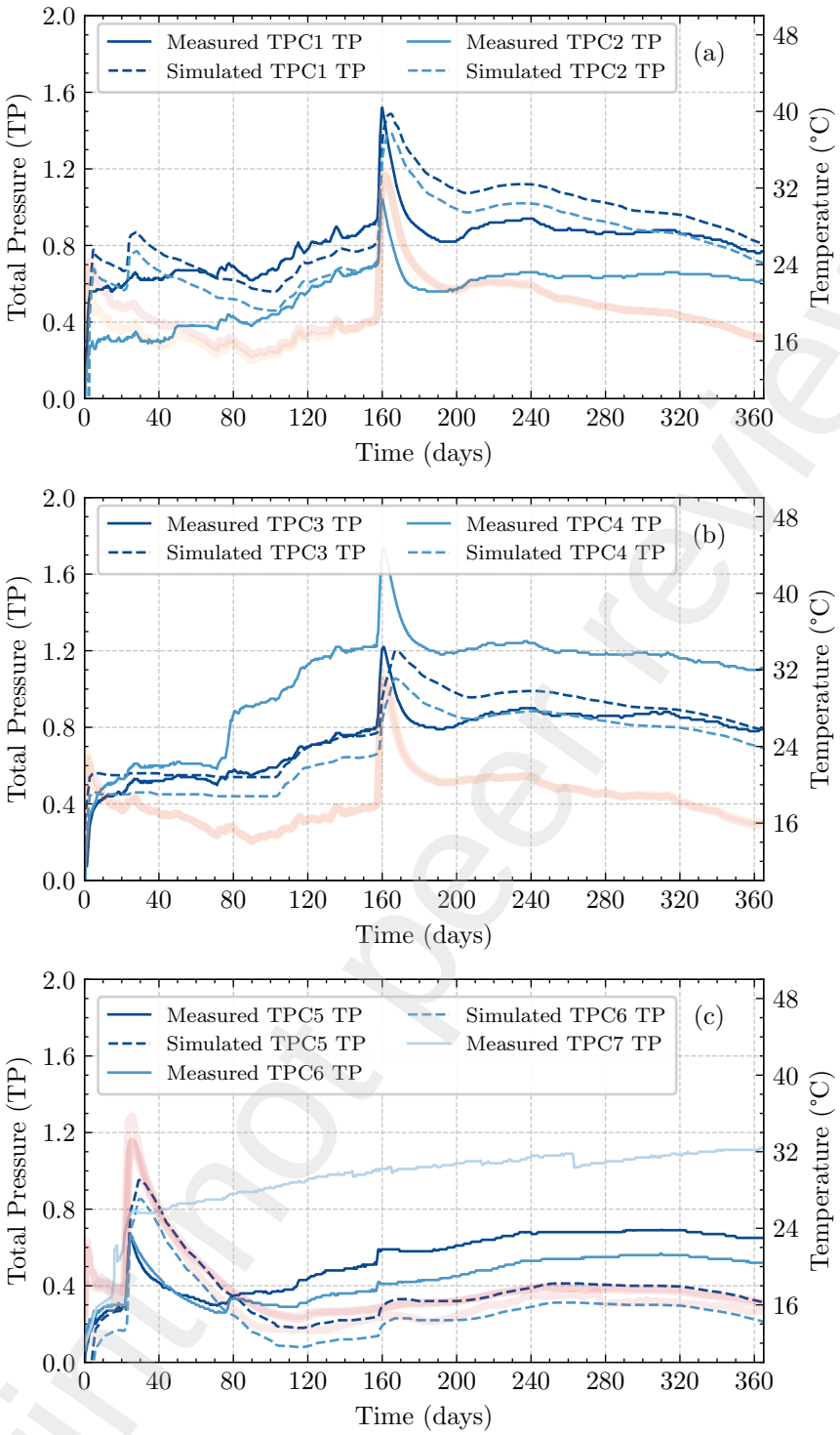

Figure 9: Temperature and Total pressure evolution in measurement points; Measured and computed data.

Figure 10a illustrates the temperature distributions computed along two distinct directions (Figure 10b) relative to a tunnel wall. The results shown correspond to day 365, marking one year since the installation of the tunnel lining. Both curves exhibit a clear trend of decreasing temperature as the distance from the tunnel wall increases, with the horizontal direction showing a slightly slower temperature decay compared to the perpendicular direction. The initial temperature near the tunnel wall is around 16.5°C, steadily declining to approximately 13°C at a distance of 20 m. The difference in temperature gradients between the two directions

highlights the anisotropic thermal behavior of the material, which may be attributed to the varying thermal properties along the tunnel axis.

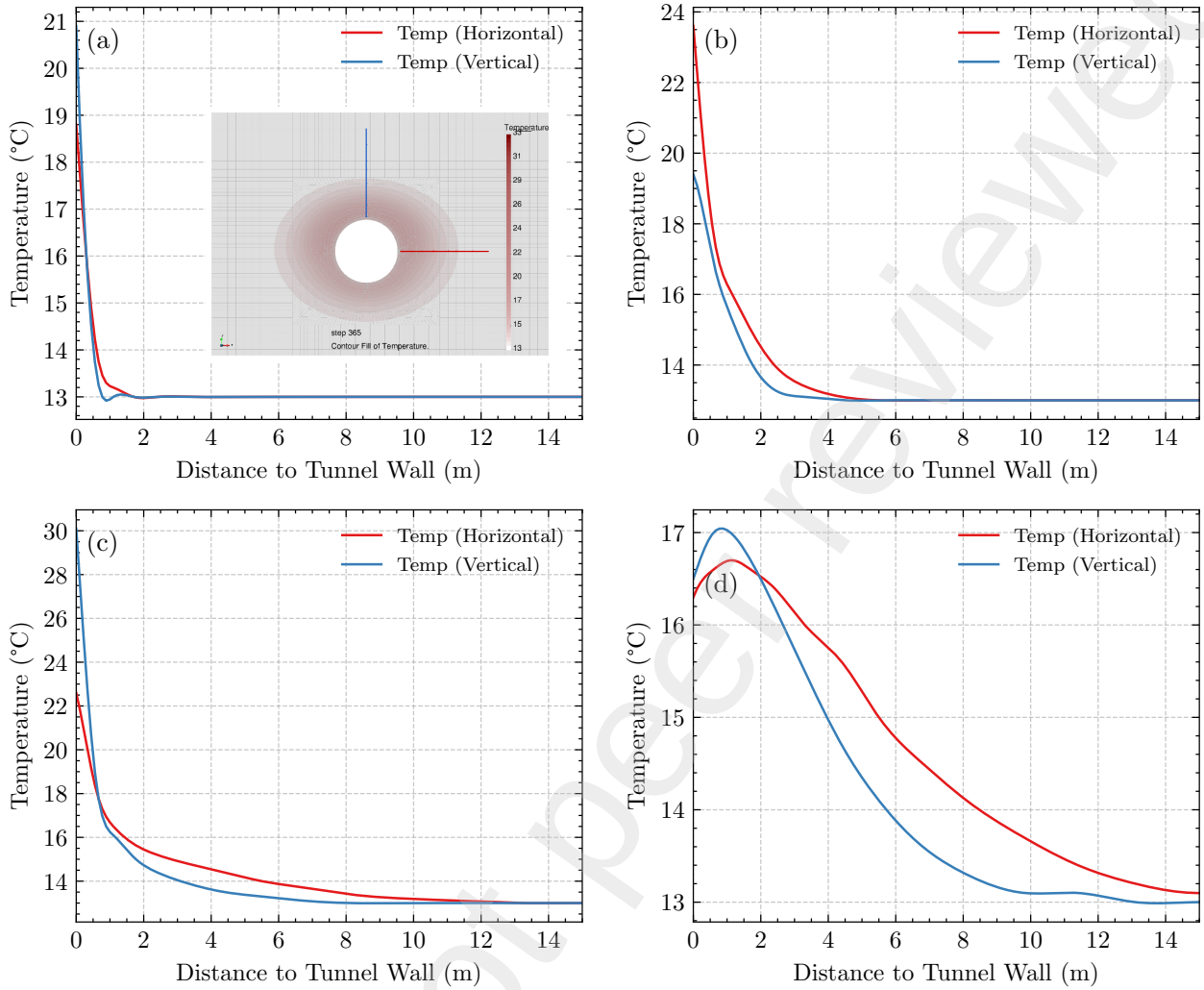

Figure 10: Computed temperature distributions at various times on bedding plane direction and perpendicular to bedding plane direction.

Anisotropic effects are more noticeable in the temperatures measured in the clay mass in terms of contours at various relevant stages (Figure 11).

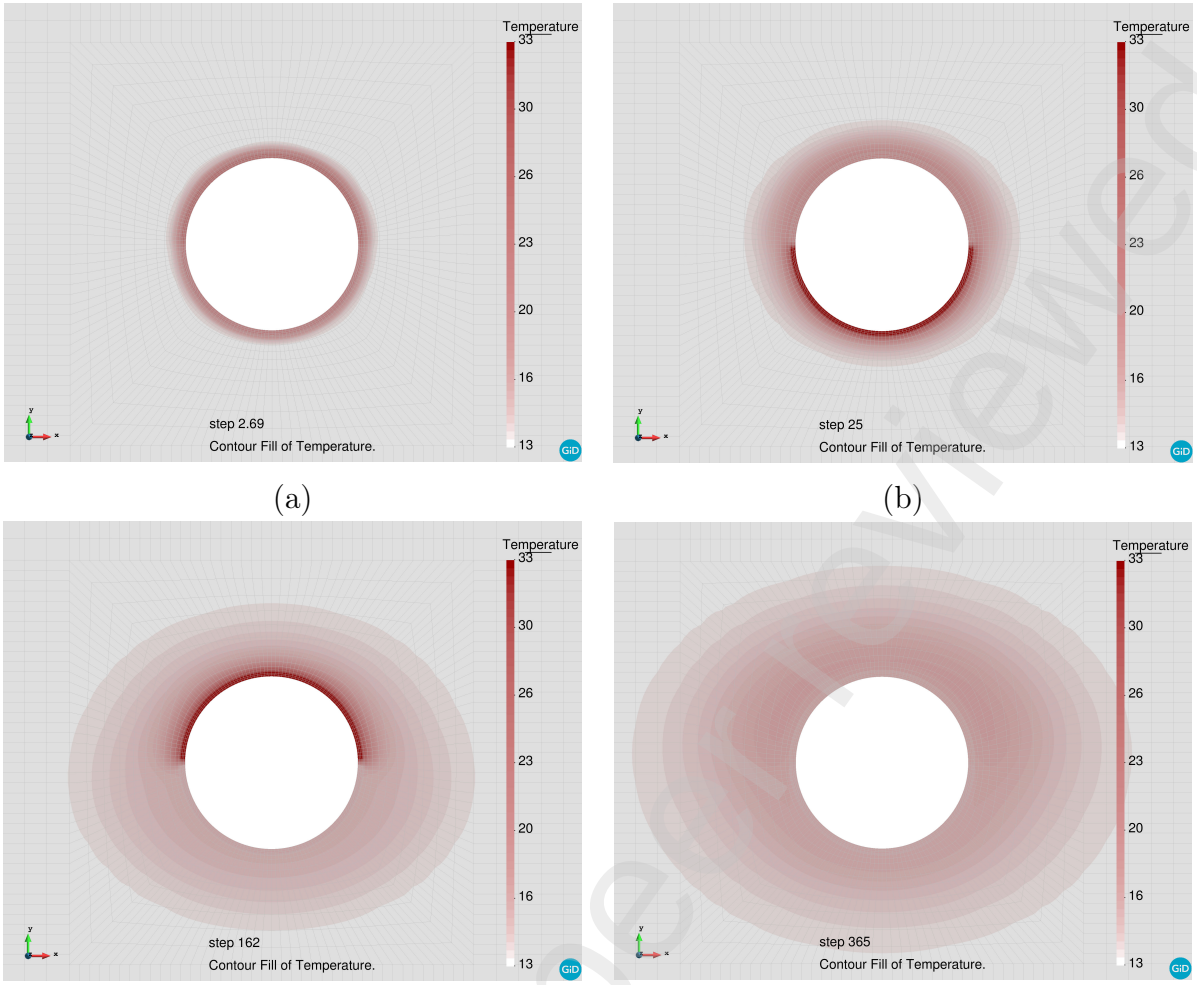

Figure 11: Computed contours of equal temperature in °C for: (a) 2.7 daysafter excavation; (b) 25 days–bottom inner liner installation; (c) 162 days– crown and sidewall support inner liner installation; (d) 365 days–end of full tunnel excavation.

Figure 12 illustrates the long-term temperature and total pressure evolution in the tunnel following the installation of the inner lining. The data reveal clear annual temperature cycles, peaking around September and reaching minima in February, closely correlating with seasonal ambient conditions. Temperature amplitudes range between 10°C to 14°C annually, with more pronounced fluctuations at the tunnel crown and sidewalls and a damped response at the invert. The observed temperature changes strongly influence the thermo-mechanical behavior of the tunnel, causing cyclic expansions and contractions that directly impact radial pressures. Figure 12 demonstrates corresponding cyclical total pressure fluctuations, peaking in late summer and reaching minima in winter. Annual pressure oscillations vary from 0.045–0.07 MPa/°C for most sensors and are lower (0.03–0.045 MPa/°C) at TPC-7. Long-term pressure increases, independent of seasonal variations, suggest underlying swelling processes in the surrounding rock mass. Spatial variability in pressure is evident, with higher pressures at the sidewalls and distinct behaviors at the crown (TPC-1 and TPC-2), influenced by construction activities such as regrouting. TPC-7 near the invert displays unique continuous pressure growth, potentially indicating pronounced swelling or localized geological activity.

Simulation results effectively capture overall trends, including seasonal thermal and pressure

fluctuations, demonstrating robust thermo-mechanical modeling capability. However, long-term pressures are underestimated due to limitations in modeling progressive rock swelling and the inherent simplifications of the two-dimensional (2D) approach, which fails to fully represent three-dimensional (3D) anisotropic and localized stress effects, notably near the cross-passage excavation. Nonetheless, the model shows satisfactory agreement with observed pressures at locations less impacted by localized complexities (e.g., TPC-1, TPC-3, TPC-5), validating the general predictive capability of the numerical approach.

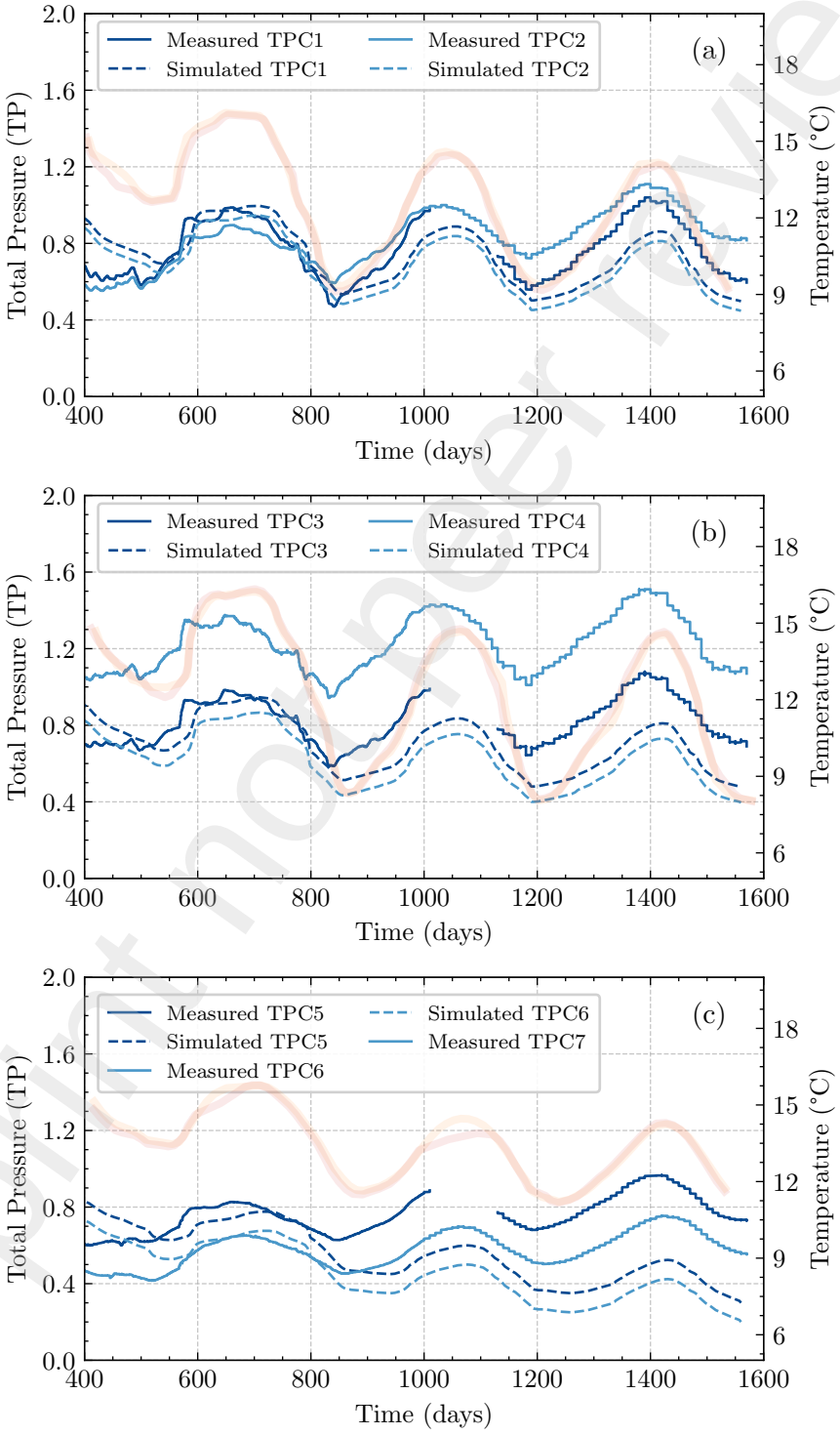

Figure 12: Temperature and total pressure evolution in measurement points during operational phases. Observed and computed values.

5.3.2 Pore pressures

The computed results in Figure 13 demonstrate the evolution of liquid pressure and temperature at various distances from the tunnel wall, along the horizontal and vertical directions.The coupled THM behavior of OPA shale surrounding a tunnel reveals key interactions between temperature and liquid pressure over time. Numerical simulation results (Figure 13) show that immediately after construction, exothermic heat induces sharp pressure increases near the tunnel wall to about 2.5 MPa in the horizontal direction (along the tunnel axis) versus 1.8 MPa in the vertical direction (perpendicular to the tunnel axis). By 25 and 162 days, the thermal front extends to 10 m, with pressures reaching 4 MPa and stabilizing at 2 MPa.

The system has largely stabilized at 365 days, as shown in Figure 13d. The temperature near the tunnel wall remains slightly elevated, but the gradient has significantly diminished. However, the liquid pressure, particularly in the horizontal direction, remains high, stabilizing around 3 MPa at the tunnel wall and gradually reducing further from the wall. The directional pore pressure dissipation differences shown in Figure 13 highlights the lasting impact of thermal expansion and anisotropic permeability aligned with the tunnel geometry. Generally, the relationship between temperature and liquid pressure is most pronounced near the tunnel wall, where the exothermic heat from construction and lining curing drives significant increases in both temperature and liquid pressure. The anisotropy of the clay plays a key role in modulating this behavior, with higher liquid pressures and slower dissipation observed along the horizontal direction.

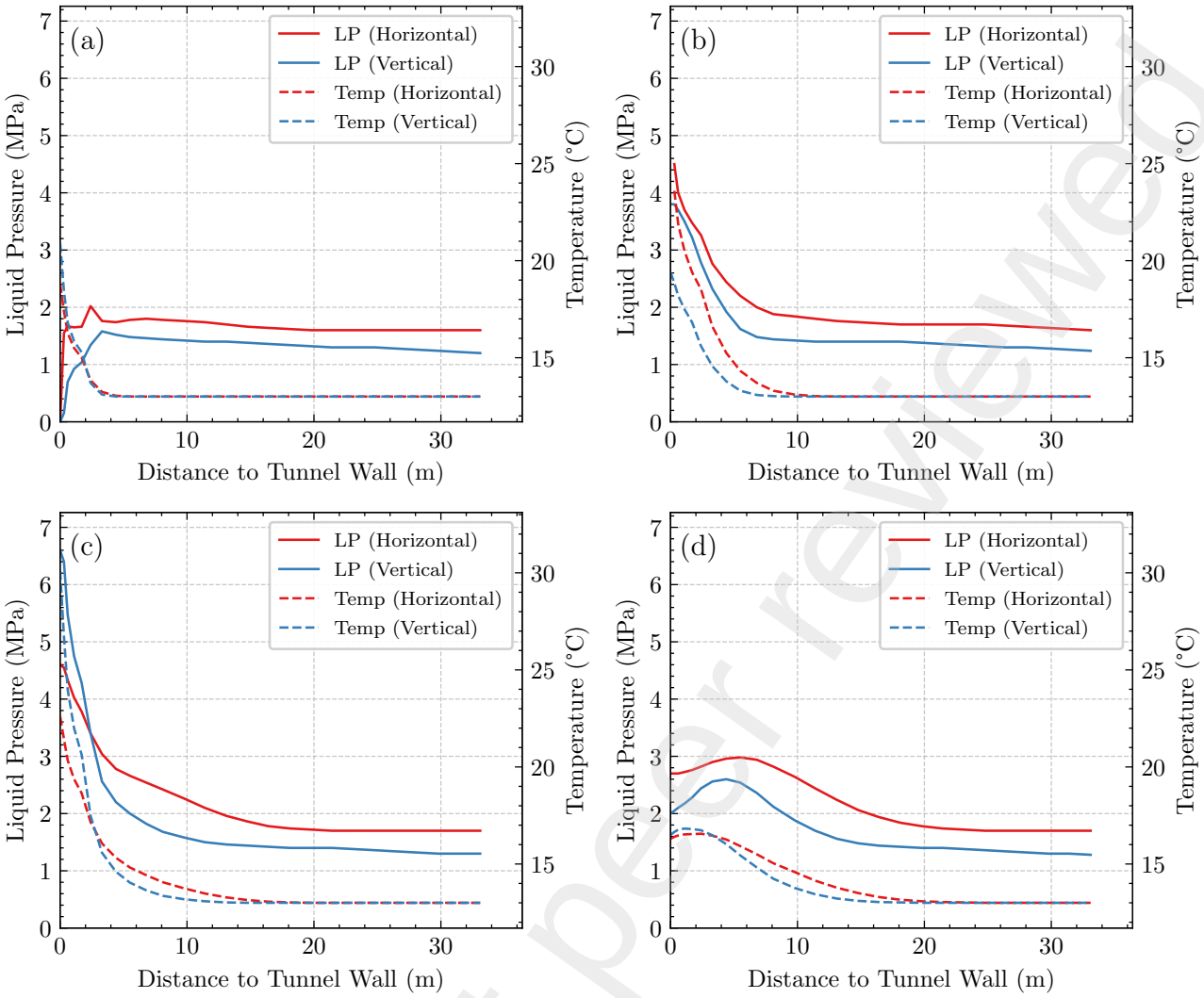

Figure 13: Computed temperature and pore pressure distributions at various times on tunnel axis direction.

Anisotropy of generated pore pressures can also be observed in the contours of equal pore pressure presented in Figure 14. The displacement of the maximum pore pressure away from the tunnel wall as time goes on is also readily apparent. In addition, it is interesting to note that, 365 days after construction, pore pressures have not yet returned to equilibrium levels around the tunnel in OPA shale. Close to the tunnel wall, pore pressures are depressed owing to the reduction brought about by cooling. In contrast, some positive excess pore pressures prevail away from the tunnel wall, where temperature changes are more gradual. These results emphasize the importance of considering both temperature and liquid pressure effects in tunnel design, particularly in anisotropic, low-permeability formations like OPA shale, where pressure dissipation can be slow and sustained thermal effects may influence the tunnel's structural integrity.

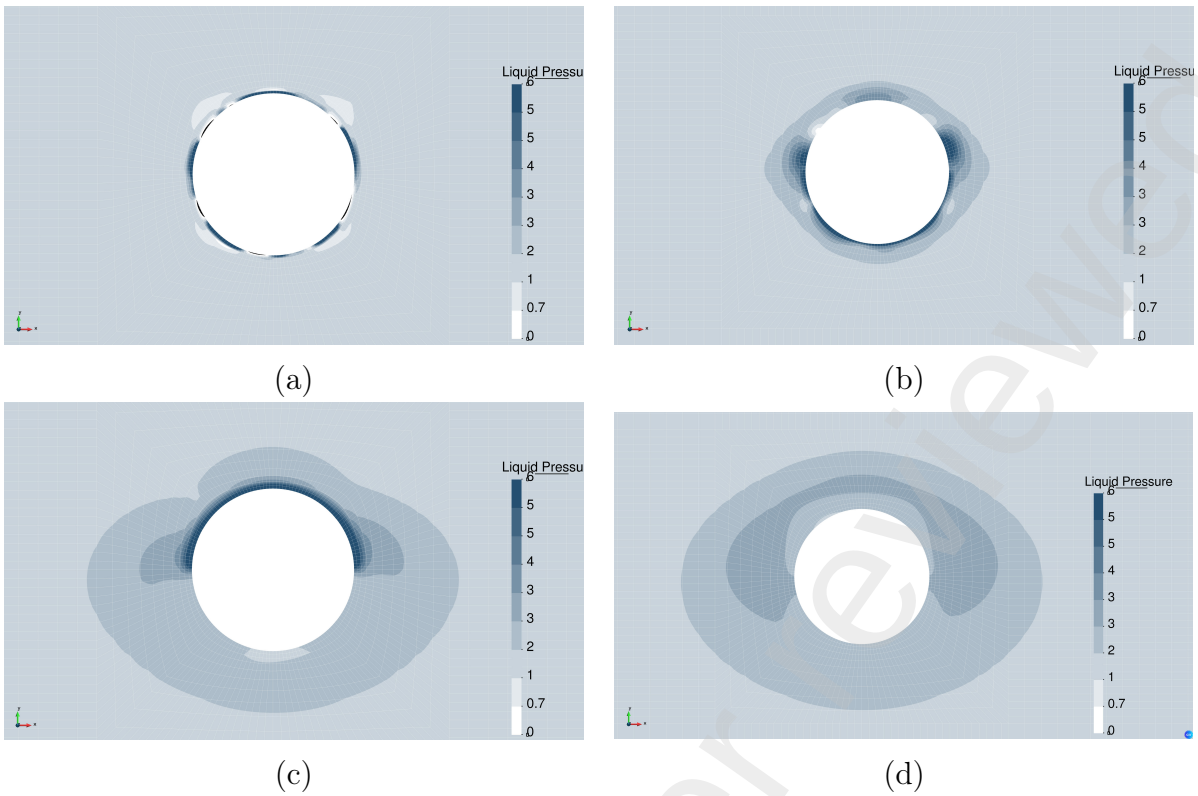

(a) (b) (c) (d)

Figure 14: Computed contours of equal liquid pressure (MPa) for: (a) 2.69 days; (b) 25 days; (c) 162 days; (d) 365 days.

5.3.3 Plastic zone

The plastic zone surrounding the excavation at various time steps is depicted in Figure 15 using the cumulative plastic multiplier, which quantifies irreversible plastic strains and reflects the extent of damage in the host rock. The OPA shale's bedding planes, dipping at 45°, introduce anisotropy within the 2D plane-strain model (x-y plane). Although the model assumes plane strain along the tunnel axis (z-direction), the 45° dip of the bedding planes relative to the horizontal (x-axis) means that the horizontal direction (x) is more aligned with the bedding planes, while the vertical direction (y) is closer to perpendicular. This orientation results in strength anisotropy within the x-y plane: the rock exhibits lower strength and greater deformability along the bedding planes (more aligned with the x-direction) compared to the perpendicular direction (more aligned with the y-direction). Consequently, the Excavation Damaged Zone (EDZ) extends more in the horizontal direction, parallel to the bedding planes, where the rock is weaker and more prone to deformation. This anisotropic behavior, driven by the bedding orientation, is captured in the model through the non-uniform scaling of the stress tensor and is critical for understanding the EDZ's development.

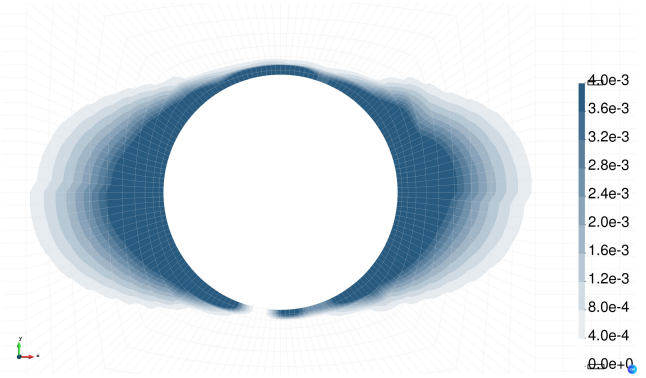

Figure 15: configuration of the EDZ in terms of the plastic multiplier for 365 days.

Figure 16 presents the spatial distribution of the computed plastic multiplier increment, EP_{mult} ,in both horizontal and vertical directions as a function of radial distance from the tunnel wall at four discrete time steps. In all cases, the highest EP_{mult} values occur adjacent to the tunnel lining and diminish rapidly with distance, indicating that plastic deformation is strongly concentrated near the excavation boundary. These findings highlight the time-dependent nature of anisotropic plasticity around underground excavations and underline the importance of temporal considerations in tunnel support design.

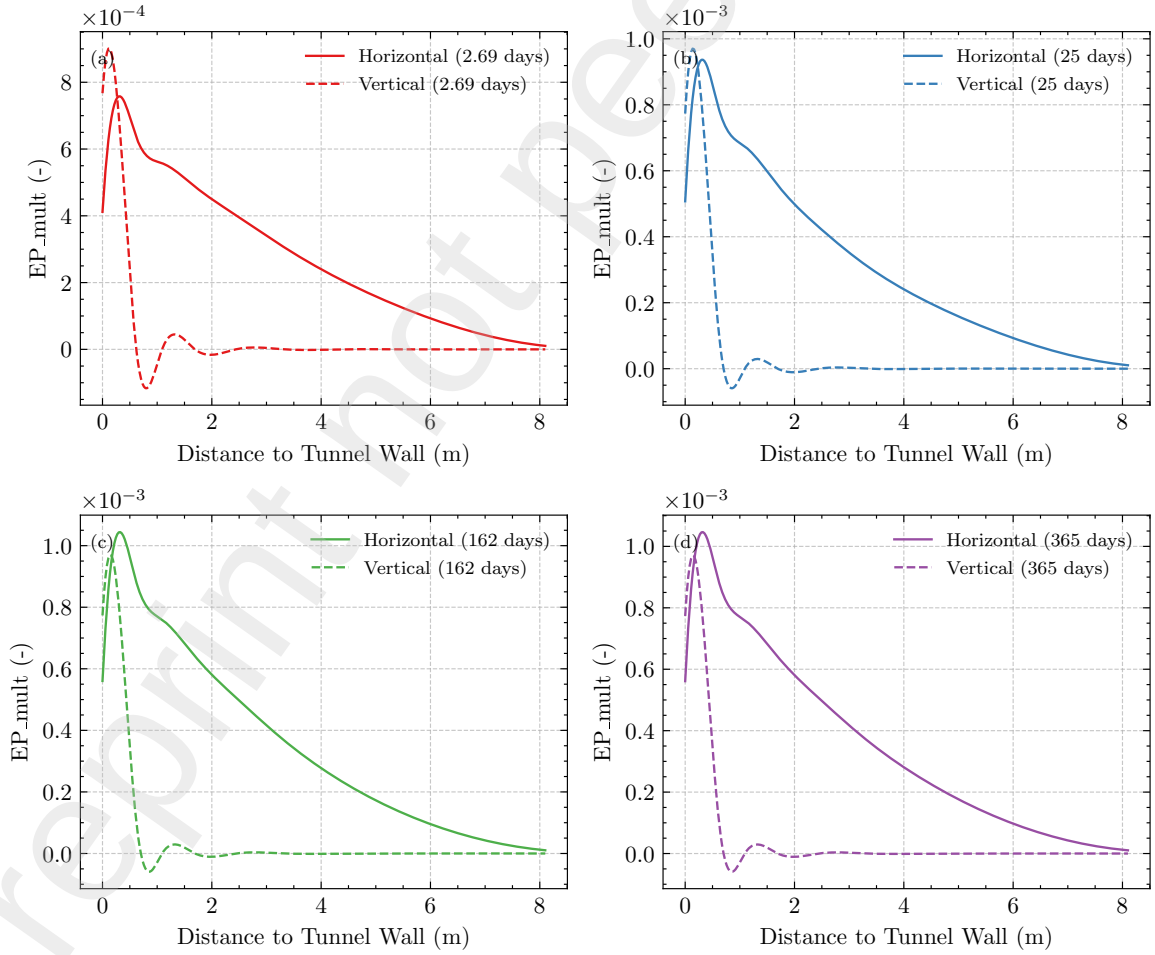

Figure 16: Computed plastic multiplier increment (EP_{mult}) distributions along the distance to the tunnel wall at different time steps. The subplots illustrate the evolution of EP_{mult} for both horizontal (solid lines) and vertical (dashed lines) directions at 4 different time steps: (a) 2.69 days, (b) 25 days, (c) 162 days, and (d) 365 days.

Figure 17 brings together the temporal evolution of EP_{mult} profiles for the horizontal (left panel) and vertical (right panel) directions. In the horizontal direction, peak EP_{mult} values increase steadily over time, with the 365-day profile exhibiting the highest amplitude and broadest spatial extent. This trend underscores the cumulative nature of plastic strain in the horizontal plane, likely reflecting a continued redistribution of deviatoric stresses in response to excavation-induced unloading. The profiles also exhibit a progressive flattening, indicative of a widening influence zone as the system evolves. In contrast, the vertical EP_{mult} profiles remain relatively stable across all time steps, with only minor variations observed between the earliest and latest stages. These observations confirm that the evolution of plastic deformation around the tunnel is both directionally dependent and time-sensitive, with important implications for the long-term assessment of tunnel stability and the optimization of support systems.

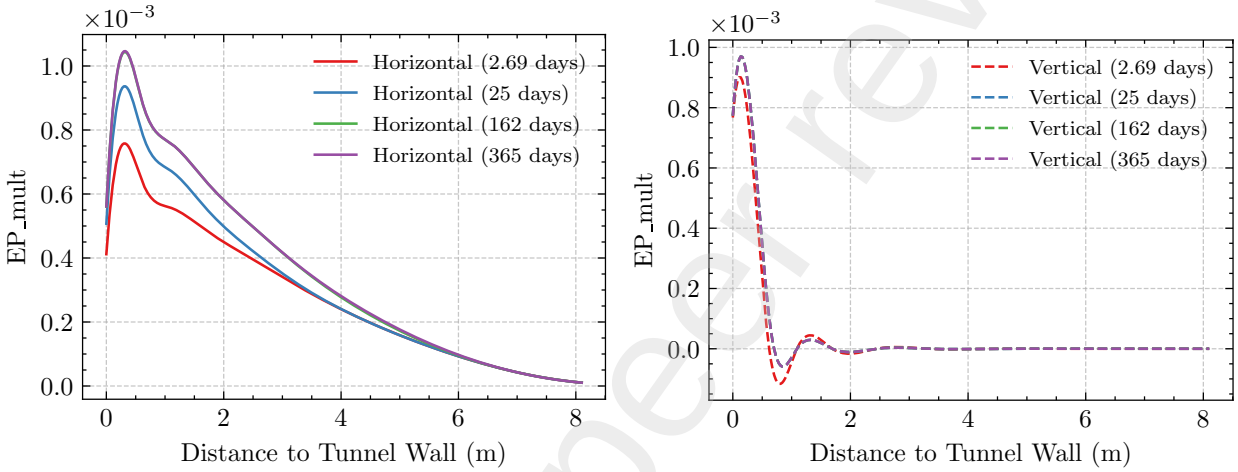

Figure 17: Computed plastic multiplier increment (EP_{mult}) distributions as a function of the distance to the tunnel wall for different time steps. Left: horizontal direction, showing EP_{mult} profiles at 2.69, 25, 162, and 365 days. Right: vertical direction, illustrating EP_{mult} profiles at the same time steps.

6 Conclusions

This study presents a comprehensive Thermo-Hydro-Mechanical (THM) analysis of the New Belchen Tunnel (STB) TBM–excavated in faulted Opalinus Clay (OPA) shale. By integrating field measurements with advanced numerical simulations, the research clarifies the critical role of coupled thermal, hydraulic, and mechanical processes in governing the tunnel's intermediate and long-term behavior. Key findings include:

- *Thermal Effects on Stress Evolution*: Temperature fluctuations driven by construction activities (e.g., grout hydration), seasonal variations, and operational heat, significantly influence radial stress redistribution. Exothermic reactions during concreting and seasonal temperature cycles induce thermal expansion mismatches between the lining and host rock, generating cyclical pressure variations (0.03–0.07 MPa/°C) and contributing to long-term stress recovery. The model demonstrates that neglecting these thermal interactions leads to underestimation of lining pressures.

- *Anisotropic Behavior*: The bedding orientation of OPA shale (dipping at 45°) introduces

pronounced anisotropy in mechanical and thermal responses. Plastic deformation and pore pressure dissipation are directionally dependent, with the horizontal axis (normal to bedding strike) exhibiting greater EDZ extent and slower pressure dissipation compared to the vertical direction. This anisotropy necessitates orientation-specific considerations in support design.

- *Pore Pressure Dynamics*: Thermal expansion under low permeability conditions generates excess pore pressures (up to 4 MPa near the tunnel wall), reducing effective stresses and potentially triggering swelling or fractures in the excavation-damaged zone (EDZ). Pore pressures remain elevated beyond one year post-excavation, highlighting the long-term hydraulic coupling effects in clay shale.

- Excavation-Damaged Zone (EDZ) Evolution: Plastic strain localization, quantified by the cumulative plastic multiplier, reveals an EDZ extending 2–3 m into the host rock, with progressive growth over 365 days. The anisotropic strength and permeability of OPA shale result in asymmetric EDZ development, emphasizing the need for time-dependent support strategies.

These findings have direct implications for tunnel design in argillaceous soft rock formations. Incorporating THM coupling in numerical models is essential for accurate prediction of lining stresses, particularly in TBM-excavated tunnels where continuous construction processes introduce rapid thermal perturbations. The study also underscores the importance of real-time monitoring to capture seasonal thermal effects and validate model predictions.

Limitations of the 2D plane-strain approach include simplified representations of 3D anisotropic effects and localized construction activities (e.g., cross-passage excavation). Future work should employ 3D modeling to better capture spatial variability and incorporate advanced constitutive laws for swelling and time-dependent fracture propagation. Long-term monitoring data beyond four years will further refine predictions of pressure stabilization and EDZ evolution. By bridging field observations with coupled numerical simulations, this research advances the understanding of THM interactions in deep tunnels, offering practical insights for infrastructure resilience and informing safety assessments for geological repositories in similar formations.

References

Amstad, C. and Kovári, K. (2001). Untertagbau in quellfähigem fels. Technical Report 52/94, 5408.01, Geotechnical Institute, ETH Zurich.

Antonioli, B. (2018). *Mechanical properties of gap grout installed in the TBM-excavated new Belchen A2 highway tunnel*. B.Sc. thesis, ETH Zurich. Pages: 63.

Armand, G., Doe, T., Piédevache, M., and Chavane, G. (2004). Permeability measurements in the excavation damaged zone in the opalinus clay at Mont Terri rock laboratory, Switzerland. *Canadian Geotechnical Conference*, pages 17–24.

Bossart, P., M. P. M. A. T. T. M. J.-C. (2002). Geological and hydraulic characterisation of the excavation disturbed zone in Opalinus Clay of the Mont Terri Rock Laboratory.

Bossart, P., Bernier, F., Birkholzer, J., Bruggeman, C., and al., e. (2017). Mont Terri Rock Laboratory, 20 years of research: introduction, site characteristics and overview of experiments. *Swiss Journal of Geosciences*, 110:3–22.

Bossart, P., Meier, P., Moeri, A., Trick, T., and Mayor, J.-C. (2002). Geological and hydraulic characterisation of the excavation disturbed zone in opalinus clay of the mont terri rock laboratory. *Engineering Geology*, 66:19–38.

Bossart, P. and Thury, M. (2008). Mont terri rock laboratory project. Pages: 194.

Bossart, P. and Thury, M. (2011). Characteristics of the Opalinus clay at Mont Terri. *Reports of the Swiss Geological Survey*, 3.

Bumbieler, F., Plúa, C., Tourchi, S., Vu, M. N., Vaunat, J., Gens, A., and Armand, G. (2021). Feasibility of constructing a full-scale radioactive high-level waste disposal cell and characterization of its thermo-hydro-mechanical behavior. *International Journal of Rock Mechanics and Mining Sciences*, 137:104555.

Einstein, H. (2000). Tunnels in Opalinus Clayshale – A review of case histories and new developments. *Tunneling and Underground Space Technology*, 15(1):13–29.

Einstein, H. and Bischoff, N. (1975). Design of tunnels in swelling rock. In *16th U.S. national symposium on rock mechanics*, pages 185–197.

Favero, V., Ferrari, A., and Laloui, L. (2016). Thermo-mechanical volume change behaviour of Opalinus Clay. *International Journal of Rock Mechanics and Mining Sciences*, 90:15–25.

Franzius, J. and Pralle, N. (2011). Turning segmental tunnels into sources of renewable energy. *Proc. Inst. Civ. Eng. – Civ. Eng.*, 164(1):35–40.

François, B., Laloui, L., and Laurent, C. (2009). Thermo-hydro-mechanical simulation of ATLAS in situ large scale test in Boom Clay. *Computers and Geotechnics*, 36(4):626–640. Publisher: Elsevier Ltd ISBN: 0266-352X.

Gens, A. (2010). Soil-environment interactions in geotechnical engineering. *Geotechnique*, 60(1):3–74.

Gens, A. (2013). On the hydromechanical behaviour of argillaceous hard soils-weak rocks. In Anagnostopoulos, A., Pachakis, M., and Tsatsanifos, C., editors, *Proceedings of the 15th european conference on soil mechanics and geotechnical engineering – geotechnics of hard soils–weak rocks*, volume 4, pages 71–118.

Gens, A., Manica, M., Vaunat, J., and Ruiz, D. F. (2017). Modelling the mechanical behaviour of Callovo-Oxfordian argillite: formulation and application. In Ferrari, A. and Laloui, L., editors, *Advances in laboratory testing and modelling of soils and shales (ATMSS)*, pages 37–44.

Gens, A., Vaunat, J., Garitte, B., and Wileveau, Y. (2007). In situ behaviour of a stiff layered clay subject to thermal loading: observations and interpretation. *Géotechnique*, 57(2):207–228.

Golchin, A., Vardon, P., and Hicks, M. (2022). A thermo-mechanical constitutive model for fine-grained soils based on thermodynamics. *International Journal of Engineering Science*, 174:103579.

Grob, H. (1972). Swelling pressure illustrated with the example of the Belchen tunnel. In *Proceedings of the international symposium for underground construction*, pages 99–119.

Hueckel, T. and Borsetto, M. (1990). Thermoplasticity of saturated soils and shales: constitutive equations. *Journal of Geotechnical Engineering*, 116(12):1765–1777.

Lavasan, A., Zhao, C., Barciaga, T., Schaufler, A., Steeb, H., and Schanz, T. (2018). Numerical investigation of tunneling in saturated soil: the role of construction and operation periods. *Acta Geotechnica*, 13:671–691.

Madsen, F. and Müller-Vonmoos, M. (1989). The swelling behaviour of clays. *Applied Clay Science*, 4(2):143–156.

Martin, C. and Lanyon, G. (2003). Measurement of in-situ stress in weak rocks at mont terri rock laboratory, switzerland. *International Journal of Rock Mechanics and Mining Sciences*, 40:1077–1088.

Mohajerani, M., Delage, P., Sulem, J., Monfared, M., Tang, A., and Gatmiri, B. (2012). A laboratory investigation of thermally induced pore pressures in the Callovo-Oxfordian claystone. *International Journal of Rock Mechanics and Mining Sciences*, 52:112–121.

Monfared, M., Sulem, J., Delage, P., and Mohajerani, M. (2011). A laboratory investigation on thermal properties of the Opalinus claystone. *Rock Mechanics and Rock Engineering*, 44(6):735–747. ISBN: 0060301101714.

Monfared, M., Sulem, J., Delage, P., and Mohajerani, M. (2014). Temperature and damage impact on the permeability of opalinus clay. *Rock Mechanics and Rock Engineering*, 47(1):101–110. ISBN: 0060301304597.

Mánica, M. A., Gens, A., Vaunat, J., Armand, G., and Vu, M. N. (2022). Numerical simulation of underground excavations in an indurated clay using non-local regularisation. Part 1: formulation and base case. *Géotechnique*, 72(12):1092–1112.

Mánica, M. A., Gens, A., Vaunat, J., and Ruiz, D. F. (2016). A cross-anisotropic formulation for elasto-plastic models. *Géotechnique Letters*, 6(2):156–162.

Naumann, M., Hunsche, U., and Schulze, O. (2007). Experimental investigations on anisotropy in dilatancy, failure and creep of Opalinus Clay. *Physics and Chemistry of the Earth, Parts A/B/C*, 32(8-14):889–895.

Olivella, S., Carrera, J., Gens, A., and Alonso, E. E. (1994). Non-isothermal multiphase flow of brine and gas through saline media. *Transport in Porous Media*, 15(3):271–293.

Olivella, S., Gens, A., Carrera, J., and Alonso, E. E. (1996). Numerical formulation for a simulator (CODE_bright) for the coupled analysis of saline media. *Engineering computations*, 13(7):87–112. Publisher: MCB UP Ltd.

Thoeny, R. (2014). *Geomechanical analysis of excavation-induced rock mass behaviour of faulted Opalinus Clay at the Mont Terri Underground Rock Laboratory (Switzerland)*. PhD Thesis.

Tourchi, S., Mánica, M. A., Gens, A., Vaunat, J., Vu, M.-N., and Armand, G. (2023). A thermomechanical model for argillaceous hard soils–weak rocks: application to THM simulation of deep excavations in claystone. *Géotechnique*, pages 1–14.

Tsang, C. F., Barnichon, J. D., Birkholzer, J., Li, X. L., Liu, H. H., and Sillen, X. (2012). Coupled thermo-hydro-mechanical processes in the near field of a high-level radioactive waste repository in clay formations. *International Journal of Rock Mechanics and Mining Sciences*, 49:31–44.

van Genuchten, M. T. (1980). A closed-form equation for predicting the hydraulic conductivity of unsaturated soils. *Soil Science Society of America Journal*, 44(5):892–898.

Wild, K. M. and Amann, F. (2018). Experimental study of the hydro-mechanical response of Opalinus Clay – Part 2: Influence of the stress path on the pore pressure response. *Engineering Geology*, 237(February):92–101. Publisher: Elsevier.

Yu, L., Weetjens, E., Vietor, T., and Hart, J. (2010). Integration of Timodaz Results Within the Safety Case and Recommendations for Repository Design. *Deliverable D14 TIMODAZ*.

Zhang, C. L., Rothfuchs, T., Su, K., and Hoteit, N. (2007). Experimental study of the thermo-hydro-mechanical behaviour of indurated clays. *Physics and Chemistry of the Earth*, 32(8–14):957–965.

Zhou, F., Xu, Q., and Liu, H. (2023). Effect of temperature on the geomechanical properties of deep sedimentary formations for nuclear waste disposal. *Environmental Earth Sciences*, 82(6):222.

Ziegler, M., Alimardani Lavasan, A., and Loew, S. (2022). Stress evolution around a TBM tunnel in swelling clay shale over four years after excavation. *Tunnelling and Underground Space Technology*, 128:104649.

Ziegler, M. and Loew, S. (2017). Investigations in the new TBM-excavated Belchen highway tunnel. Program, design and installations (Part 1). Technical Report ENSI-AN-9961, ENSI Research and Experience Report 2016.

Ziegler, M. and Loew, S. (2018). Investigations in the new TBM-excavated Belchen highway tunnel. Final installations and first results (Part 2). Technical Report ENSI-AN-10294, ENSI Research and Experience Report 2017.

Ziegler, M., Lukovic, M., Lavasan, A., Christ, F., Schoen, M., and Loew, S. (2021). Investigations in the new TBM-excavated Belchen highway tunnel. Status update (Part 5). Technical Report ENSI-AN-11061, ENSI Research and Experience Report 2020.

List of Figures

List of Tables